Terahertz (THz) Spectroscopy

by

NAGLA NUMAN ALI NUMAN

Thesis presented in partial fulfilment of the
academic requirements for the degree of
Master of Science in Physics
at Stellenbosch University

Supervisor: Prof. E. G. **Rohwer**
Co-supervisors: Prof. H. P. H. **Schwoerer**
Dr. C. M. **Steenkamp**
Dr. P. H. **Neethling**
Department of Physics
University of Stellenbosch
December, 2012

Declaration

By submitting this thesis electronically, I declare that the entirety of the work contained therein is my own, original work, that I am the sole author thereof (save to the extent explicitly otherwise stated), that reproduction and publication thereof by Stellenbosch University will not infringe any third party rights and that I have not previously in its entirety or in part submitted it for obtaining any qualification.

December 2012

Abstract

Terahertz radiation is currently used in security, information and communication technology (ICT), and biomedical sciences among others. The usability of terahertz (THz) radiation, in many of its applications depends on characteristics of the materials being investigated in the THz range. At the heart of THz usage is a THz spectroscopy system necessary for the generation and detection of the THz radiation. In this thesis, we characterise such a THz spectroscopy system. In our typical THz spectrometric system, we make use of femtosecond (fs) laser technology and pump-probe principles for emission and detection of THz radiation. Background about the principles of generation THz radiation using fs triggered antennas and the principles of the spectroscopy technique and appropriate literature references are presented. Using an assembled commercially available kit, we reproduce known spectra in order to confirm correct functionality (for calibration) of the assembled spectroscopy system and to gain experience in interpreting these spectra. By introducing a suitable $x - y$ scanning device we construct a crude THz imaging device to illustrate the principle.

Opsomming

Terahertsstraling word deesdae wyd in die sekuriteits, inligting-en-kommunikasie en biomediese sektore aangewend. Die gepastheid van terahertsstraling (THz) vir 'n spesifieke toepassings hang af van die eienskappe van die materiale wat ondersoek word. Vir die uitvoer van sulke eksperimente word 'n THz-spektroskopie sisteem benodig vir die opwekking en meting van THz-straling. In hierdie tesis word so 'n THz-spektroskopie sisteem beskou en gekarakteriseer. In die sisteem word van 'n femtosekondelaser (fs) gebruik gemaak in 'nn pomp-en-proef opstelling vir die uitstraling en meting van THz-straling. Die beginsels rakende die opwekking van THz-straling, deur gebruik te maak van 'n antenna wat deur 'n fs-laser geskakel word, asook die beginsels van die spektroskopiese tegniek, met toepaslike verwysings, word in die tesis aangebied. Deur gebruik te maak van'n kommersiële THz opstelling is bekende spektra gemeet om die korrekte funksionering (vir kalibrasie doeleindes) na te gaan en om ondervinding op te doen in die interpretasie van hierdie spektra. 'n X-Y-translasie toestel is tot die opstelling bygevoeg om THz-afbeelding moontlik te maak en sodoende hierdie beginsel te illustreer.

Dedication

To the family of Mr Numan Ali and my mum Safia Mansour, the source of endless love and support.

Acknowledgements

First of all, I would like to thank my advisor, Professor Erich Rohwer, I appreciate your wisdom, guidance, and support during this project. You are a great advisor and scientist. Thank you for giving me the precious opportunity to work under your direction. I would like to extend my sincere heartfelt gratitude to Dr Pieter Neethling for guiding me at critical stages of the project with brilliant ideas and solutions. My appreciation to my co-supervisors, Prof. Schwoerer and Dr Christine Steenkamp for your continued advice and guidance, during the entire project. My thanks to the entire Laser Research Institute staff for making my life at Stellenbosch University enjoyable. I would like to thank my parents, my sister and my brothers, without your constant support during this project, I could not be where I am.

Lastly, I acknowledge with gratitude the support from the University of Stellenbosch and the African Institute for Mathematical Sciences who jointly funded this project.

Contents

List of Figures

List of Tables

Chapter 1

Introduction

1.1 What is THz radiation?

The Terahertz (THz) radiation regime lies between the microwave and infrared frequencies [1]. Radiation at 1 THz has a period of 1ps, wavelength $\lambda = \frac{c}{\nu} = 300$ μm, where c is the speed of light in vacuum and ν its frequency, wavenumber $\bar{\kappa} = \frac{\kappa}{2\pi} = \frac{1}{\lambda} = 33$ cm^{-1}, photon energy $h\nu = \hbar\omega = 4.1$ meV, where h is Plank's constant [2, 3]. This equivalence relation, and location of the Terahertz band on the electromagnetic spectrum is indicated in Figure 1.1.

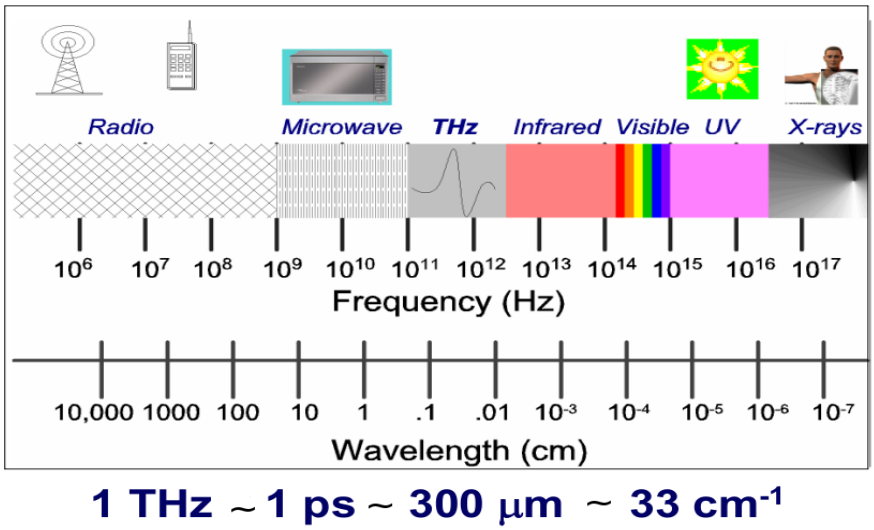

Figure 1.1. Frequency and wavelength regions of the electromagnetic spectrum [3].

In general the THz region covers the frequency range from 0.1 to 10 THz [2, 4], which is between the microwave and infrared regions of the electromagnetic spectrum [1, 2, 4]. There are two major groups of terahertz systems namely, continuous wave (CW) and pulsed terahertz systems. Pulsed THz systems refer commonly to those which generate, propagate, and detect transient electromagnetic pulses. The pulse information is taken in the time domain, and can be transformed into frequency domain by Fourier transformation [3].

With respect to the history of electromagnetic waves, research on electromagnetic waves was divided into two different fields: optical and electrical waves. We now give some differences between the two fields with reference to the emission, measurement and the tools used.

	Electrical wave	Optics
Emission	Classical dipole	Quantum transition
Measurement	Electric Field	Intensity
Tools	Circuit, antenna, waveguide	Lens, mirror, fibre

Table 1.1. Source:[3]. Comparison of Optical and Electrical waves.

The principles, methods, and tools used to deal with optical and electrical waves are very different, as presented in Table 1.1 above. On the other hand, THz waves do not simply fit within either category. Therefore, new principles, new technologies and new tools must be developed in order to understand and utilize THz waves [3]. Generation and detection of radiation forms an integral part of both an optical and an electromagnetic wave system.

In Figure 1.2 below, we compare the mechanism of generation of electrical waves and optical waves. The angular frequency of the radiation from a quantum transition is given by $\omega = \frac{\Delta E}{\hbar}$, where ΔE is the difference in energy between the two quantum levels and $\hbar$ is $\frac{h}{2\pi}$. The angular frequency of the radiation from a classical dipole is given by $\omega = \frac{1}{\sqrt{LC}}$, where C is capacitance and L is inductance. THz waves can be generated by classical dipole oscillations. Since we are interested in the electromagnetic power spectrum in the THz range, the duration of the electromagnetic oscillation is kept within picoseconds [3]. These electromagnetic oscillations in the classical dipole case follow the same principle of damped oscillations in the RLC circuit, which is described in detail in Chapter 2.

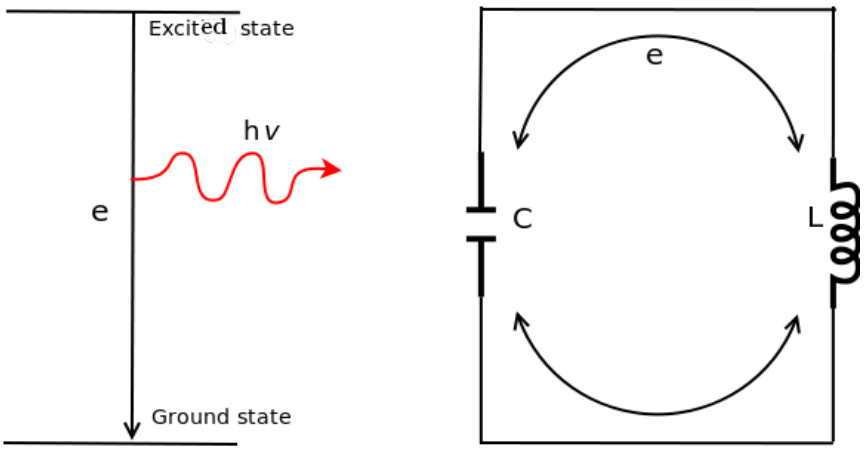

Figure 1.2. (a) Quantum transition with a photon emitted and (b) classical dipole with electromagnetic waves emitted [3].

1.2 History and background of Terahertz radiation

The concept of THz radiation is often called "sub millimetre waves" or "far infrared", revealing either an electronic or an optical approach [5]. The THz range/gap had not been studied until only recently, due to difficulties in generation and detection of THz radiation [6]. For example according to Seigel (2003) [7], THz is broadly applied to submillimetre-wave energy that fills the wavelength range between 1000 and 100 microns (300 GHz to 3 THz). However, in recent research work, it is commonly referred to lie between the microwave and infrared region, with a spectral range of 0.1-10 THz [2, 6, 8] or 0.3-10 THz [9, 10, 11] on the electromagnetic spectrum.

Although great scientific interest in the THz frequency range has existed only since the 1920s [7], this frequency range has been investigated for more than 120 years now [12]. However, the THz frequency range remains one of the least tapped regions of the electromagnetic spectrum [7]. This is most probably due to the difficulty in generating and detecting the THz radiation, and hence the spectroscopy kits used are expensive. Terahertz did not come into popular use until the mid 1970s, where it was employed by spectroscopists to describe emission or absorption frequencies that fell below the far infrared (IR) [7]. Early work began in the late 1970s and early 1980s with the study of the response of photoconductors (PC) to laser pulses. The first archetypes of photoconductive

antennas (as THz emitters and detectors) were used in the late 1980s. Since then, these devices have remained widely used in the generation and detection of the THz radiation [3].

The earliest work on the application of THz radiation was in spectroscopy. Most of the current work focuses more on imaging in biomaterial identification, detection of cancerous cells, oral health care, dermatology, DNA molecular structure among others. Since imaging provides more information about the shape and structure, and spectroscopy provides more information about the chemical composition, the successful application of THz seems to be a combination of the two [5]. Most of the imaging is done on materials with low water content since liquid water and all wet materials, including most biological tissues, have a very strong absorption coefficient in the THz range, about 10^6 times higher than in the visible range [5].

Terahertz systems are mainly pulsed systems with photoconductive switches as the emitters and detectors of the radiation. Low-temperature gallium arsenide (LT-GaAs) has been the most widely used material in pulsed systems for the photoconductive emitter and detector because of its unique properties, such as the ultrashort carrier lifetime, large resistivity, and relatively good carrier mobility [13].

1.3 Applications of THz radiation

The applications of THz radiation exploit the response of materials to fundamental physical processes such as rotational transitions in molecules, large-amplitude vibrational motions of organic compounds and lattice vibrations in solids [2]. The atmosphere within the THz radiation path usually contains molecules with rotational lines in the THz band which result in high opacity when compared with neighbouring regions such as radio wave and infrared radiation. The high opacity in the THz band is particularly due to absorption by water vapour in the atmosphere causing THz attenuation.

Different materials of condensed matter exhibit different properties in the THz range. Here we give summary of the most important properties of some materials in Table 1.2.

Material type	Optical property
liquid water	high absorption ($\alpha = 250 \quad \text{cm}^{-1}$ at 1 THz)
metal	high reflective (> 99.5 % at 1 THz)
plastic	low absorption ($\alpha < 0.5 \quad \text{cm}^{-1}$), low refractive index ($n \cong 1.5$)
semiconductor	low absorption ($\alpha < 1 \quad \text{cm}^{-1}$ at 1 THz), high refractive index ($n \cong 3.4$)

Table 1.2. Source [2]: Optical properties of condensed matter in the THz band.

1.3.1 Security

THz spectroscopy has found wide application in the industry, most noticeably in airport terminals to curb drug trafficking and terrorism. Explosives and narcotics have distinct absorption signatures in the THz region [14]. This allows identification and distinguishing of chemicals, illicit drugs and explosives from licit and benign compounds. Metallic substances are highly reflective at THz frequencies because of their high electrical conductivity [2]. This property is vital in detecting and tracing the exact shapes of hidden guns, ammunitions, and sharp instruments such as knives. THz can pass through paper, ceramics, wood and clothing. Materials hidden under clothes can be identified using THz multispectral imaging and those in envelopes can be identified by component spatial-pattern analysis without opening the envelopes [6].

1.3.2 Biological and pharmaceutical sciences

Terahertz time domain spectroscopy (THz-TDS) has immense applications in sensing and information communication technology. The sensing capabilities have been applied to many materials such as biomolecules, medicines, cancer tissue, DNA, proteins and bacteria [14]. THz radiation is non-invasive, and hence it can be a good substitute for X-rays in imaging live cells. The various examples of THz application in the biomedical field include dermatology in the characterisation of the hydration-level of the stratum corneum [11], dentistry to detect dental cavities [11, 15], oncology (skin cancer) by distinguishing base cell carcinomas from other normal cells [11, 14, 15, 16]. In pharmaceutical industries, THz imaging is used to check the integrity of tablet coatings and the performance of tablet cores [11]. THz rays have also been used to study the binding state of DNA molecules and distinguishing the hybridised and denatured DNA with considerable progress towards the

development of label-free DNA chips [11, 14, 15].

1.4 Objectives of the study

The objectives of this study are to:

1. give a brief description of THz radiation, its properties, and some processes by which it can be generated,
2. give an understanding of the theory of the electric circuit of the THz spectroscopic system,
3. describe the generation and detection of THz radiation using a photoconductive antenna,
4. describe THz radiation as an electromagnetic wave and consider its transmission through and reflection from example materials, and to
5. produce and interpret the spectra of example materials and give some applications of THz radiation in imaging, health and security.

1.5 Outline of the thesis

In Chapter 1, we give a brief introduction to THz radiation, the general differences between electrical and optical waves and some historical background to THz radiations.

In Chapter 2, we discuss the general theory of the RC and RLC circuits with the main emphasis on the different types of damping and the flow of current and the electric field generated by the circuit.

The background theory, which is necessary for understanding the generation and detection of the THz radiation using a photoconductive antenna is discussed in Chapter 3. In Chapter 3, we also describe the experimental technique and several ways used in generating and detecting the THz pulse. In this thesis the main focus is on the generation and detection of

THz radiation, using a photoconductive switch. It is in this chapter where we present the materials used in photoconductive switches, the description of the Terahertz time domain spectroscopic technique, the theory of THz radiation as an electromagnetic wave and THz radiation and detection using a photoconductive antenna.

Chapter 4 is devoted to describing the experimental setup used, windows/lenses, the materials used for making lenses and finally some optical properties of solids. In Chapter 5, we discuss the Fourier transform as a means to relate the time and frequency dependence of the voltage across a capacitor in an RLC circuit, and we describe the absorption and transmission of radiation through materials and waveform measurements of THz pulses through materials. In Chapter 6, we give the summary and general conclusion to our work.

Chapter 2

Theory of the electric circuit to generate THz radiation

The electric circuit of a THz spectroscopic system has a small capacitor with capacitance C and bias voltage V. The energy stored in the capacitor is given as $E_{\text{capacitor}} = \frac{1}{2}CV^2$. When the circuit is closed the energy stored is discharged. Part of this energy is radiated into a THz pulse and the rest is released as heat. To understand the theory of the THz spectroscopic system, it is necessary to know the theory of its electric circuit. We therefore give a brief review of the theory behind the RC and RLC circuits and investigate the flow of current through the circuit for different damping cases.

2.1 RC circuits

An RC circuit is composed of a capacitor (capacitance C) and a resistor (resistance R) connected in series, and the voltage across the capacitor is given by [17]

$$\varepsilon = iR + \frac{1}{C}q. \tag{2.1}$$

This equation has two variables, the current i and the charge q, which are not independent but are related by

$$i = \frac{dq}{dt}. \tag{2.2}$$

Substituting equation (2.2) into equation (2.1), we obtain

$$R\frac{dq}{dt} + \frac{q}{C} = \varepsilon. \tag{2.3}$$

This differential equation describes the variation of charge q in a capacitor with time [17]. The solution of the first order differential equation (2.3) is obtained by using a suitable integrating factor $\left(e^{\frac{1}{RC}t}\right)$ and is given by

$$q = C\varepsilon(1 - e^{-t/RC}). \tag{2.4}$$

The charge q and the potential difference V of the capacitor are proportional, and the relation is given by [17]

$$q = CV_c, \tag{2.5}$$

where C is the capacitance of the capacitor. Substituting equation (2.4) into equation (2.5), we obtain

$$V_c = \varepsilon(1 - e^{-t/RC}). \tag{2.6}$$

We can measure V_R, the potential difference across the resistor by measuring $i(t)$ and use Ohm's law given as

$$V_R = iR. \tag{2.7}$$

Substituting $i = \frac{dq}{dt}$ into equation (2.7), we obtain the explicit expression for voltage across the resistor as

$$V_R = \varepsilon e^{-t/RC}. \tag{2.8}$$

2.2 RLC circuits

To investigate the current through an RLC circuit, we use a series RLC circuit as in Figure 2.1. We let the capacitor have an initial voltage V_0 and the inductor an initial current of zero. When the switch is closed at time $t = 0$, current starts to flow in the circuit due to the initial stored energy in the capacitor. The voltage across the capacitor starts from some initial value V_0 and decays.

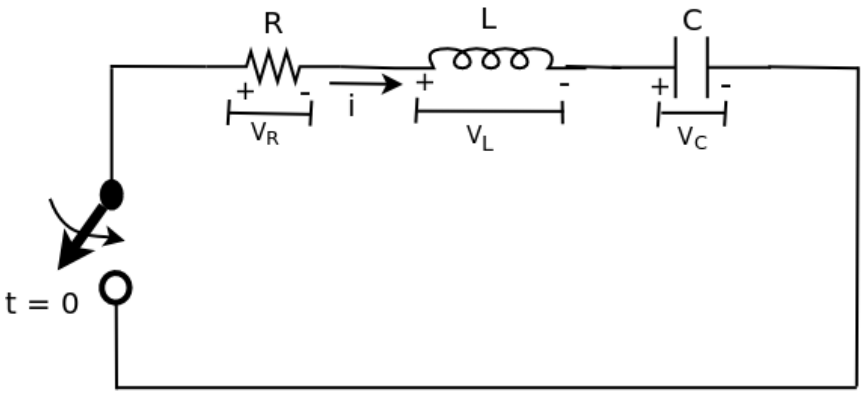

Figure 2.1. Schematic diagram for a series RLC circuit.

The differential equation [18] describing the change in current is given by

$$L\frac{di(t)}{dt} + Ri(t) + \frac{1}{C}\int i(t)dt = 0. \tag{2.9}$$

Differentiating equation (2.9), we obtain

$$\frac{d^2i(t)}{dt^2} + \frac{R}{L}\frac{di(t)}{dt} + \frac{1}{LC}i(t) = 0. \tag{2.10}$$

The resulting homogeneous differential equation (2.10) has a solution of the form (2.11) [18]

$$i(t) = ke^{nt}, \tag{2.11}$$

where k and n are constants. Now substituting equation (2.11) into (2.10), we obtain the quadratic equation given by

$$n^2 + \frac{R}{L}n + \frac{1}{LC} = 0. \tag{2.12}$$

Equation (2.12) has two solutions n_1 and n_2, given by

$$n_1 = \frac{-R}{2L} + \sqrt{\frac{R^2}{4L^2} - \frac{1}{LC}} \quad \text{and,} n_2 = \frac{-R}{2L} - \sqrt{\frac{R^2}{4L^2} - \frac{1}{LC}}.$$

Depending on the values of R, L and C, there are three possible cases as described below :

Case(1): when $\frac{R^2}{4L^2} = \frac{1}{LC}$, then $n_1 = n_2 = (\frac{-R}{2L})$ (repeated roots).

Case(2): when $\frac{R^2}{4L^2} > \frac{1}{LC}$, then n_1 and n_2 are real and not equal (distinct roots).

Case(3): when $\frac{R^2}{4L^2} < \frac{1}{LC}$, then n_1 and n_2 are complex conjugates.

In case (1), the solution for (2.11) is given by

$$i(t) = (k_1 t + k_2)e^{-(\frac{R}{2L})t}. \tag{2.13}$$

In cases (2) and (3), the solution in (2.11), is given by

$$i(t) = k_1 e^{n_1 t} + k_2 e^{n_2 t}, \tag{2.14}$$

when $n_1 \neq n_2$. From the initial conditions we can find the coefficients n_1 and n_2. There are two initial conditions, current continuity across the inductor and voltage continuity in the capacitor as respectively described below;

$$i(0+) = i(0-) = 0, \tag{2.15}$$

$$V_c(0+) = V_c(0-) = V_0. \tag{2.16}$$

The Kirchhoff's voltage law (KVL) equation of the circuit in Figure 2.1, is given by

$$V_R + V_L + V_C = 0. \tag{2.17}$$

When $t = 0, i = 0$, therefore, $V_R(0) = 0$.

Using the conditions (2.15) and (2.16) and equation (2.17) we obtain

$$V_L(0) = -V_C(0) = -V_0. \tag{2.18}$$

Since $V_L(t) = L\frac{di}{dt}$, the initial value of the derivative $\frac{di}{dt}$ is given by

$$\frac{di}{dt} = \left(\frac{V_L}{L}\right), \quad \text{at} \quad t = 0. \tag{2.19}$$

Now we use two initial conditions (2.15) and (2.16) to find the coefficients k_1 and k_2, from equations (2.13) and (2.14).

Case (1): Critically damped RLC circuit.

When $R = 2\sqrt{\frac{L}{C}}$: Recall that $n_1 = n_2$ and the general equation for the flow of current is given by equation (2.14). Therefore, using the initial condition (2.15) we obtain

$$k_2 = 0. \tag{2.20}$$

Then substitute equation (2.20) into equation (2.14), we obtain

$$i(t) = k_1 t e^{-(\frac{R}{2L})t}. \tag{2.21}$$

To find the constant k_1, we differentiate equation (2.21), to obtain

$$\frac{di(t)}{dt} = k_1 e^{-(\frac{R}{2L})t} - \left(\frac{R}{2L}\right) k_1 t e^{-(\frac{R}{2L})t}. \tag{2.22}$$

Then we substitute $t = 0$ and $\frac{di}{dt} = -\left(\frac{V_0}{L}\right)$, in equation (2.22), to obtain the expression for k_1 and hence $i(t)$ as

$$k_1 = -\frac{V_0}{L} \quad \text{and,} \tag{2.23}$$

$$i(t) = -\left(\frac{V_0}{L}\right) t e^{-(\frac{R}{2L})t} \quad \text{respectively.} \tag{2.24}$$

This describes the flow of current in a critically damped circuit. In Figure 2.3, it can be observed that the current first increases to the maximum and thereafter decays to zero [18].

Case (2): Over damped RLC circuit.

When $R > 2\sqrt{\frac{L}{C}}$, the current is given by

$$i(t) = k_1 e^{n_1 t} + k_2 e^{n_2 t}, \tag{2.25}$$

where n_1 and n_2 the distinct roots are given by

$$n_1 = \frac{-R}{2L} + \sqrt{\frac{R^2}{4L^2} - \frac{1}{LC}}, \quad \text{and} \tag{2.26}$$

$$n_2 = \frac{-R}{2L} - \sqrt{\frac{R^2}{4L^2} - \frac{1}{LC}} \quad \text{respectively.} \tag{2.27}$$

We now use the initial condition $i(+0) = 0$ in equation (2.25), to obtain

$$k_1 + k_2 = 0. \tag{2.28}$$

Differentiating equation (2.25) and substituting $t = 0$ and $\frac{di}{dt} = -\left(\frac{V_0}{L}\right)$, we obtain

$$n_1 k_1 + n_2 k_2 = -\frac{V_0}{L}. \tag{2.29}$$

Substituting equation (2.28) into equation (2.29), we now obtain the constants

$$k_1 = -k_2 = \frac{V_0}{L(n_1 - n_2)}. \tag{2.30}$$

We now substitute the constants k_1 and k_2 from equation (2.30) into equation (2.25), to obtain the expression for the flow of current as

$$i(t) = \frac{V_0}{L(n_1 - n_2)} \left[e^{n_2 t} - e^{n_1 t}\right]. \tag{2.31}$$

Figure 2.3 shows that the current in an over damped RLC circuit has a similar trend as that in a critically damped circuit.

Case (3): Under damped RLC circuit.

When $R < 2\sqrt{\frac{L}{C}}$, then the discriminants of n_1 and n_2 are negative. Therefore, the roots n_1 and n_2 are complex conjugates and are given by

$$n_1 = \frac{-R}{2L} + j\sqrt{\frac{R^2}{4L^2} - \frac{1}{LC}}, \text{ where } j^2 = -1, \tag{2.32}$$

$$n_2 = \frac{-R}{2L} - j\sqrt{\frac{R^2}{4L^2} - \frac{1}{LC}}. \tag{2.33}$$

If we let $\alpha = \frac{R}{2L}$ and $\beta = \sqrt{\frac{R^2}{4L^2} - \frac{1}{LC}}$, then

$$n_1 = -\alpha + j\beta, \quad \text{and} \quad n_2 = -\alpha - j\beta. \tag{2.34}$$

The current is given by

$$i(t) = k_1 e^{-(\alpha - j\beta)t} + k_2 e^{-(\alpha + j\beta)t}. \tag{2.35}$$

To find the constants k_1 and k_2, we use $i(0+) = 0$ in equation (2.35), to obtain

$$k_1 + k_2 = 0. \tag{2.36}$$

We then differentiate equation (2.35) and evaluate $\frac{di}{dt}$ at $t = 0$ to obtain

$$(-\alpha + j\beta)k_1 - (\alpha + j\beta)k_2 = -\left(\frac{V_0}{L}\right). \tag{2.37}$$

Solving equations (2.36) and (2.37) simultaneously, we obtain

$$k_1 = -k_2 = -\frac{V_0}{2j\beta L}. \tag{2.38}$$

Then substituting equation (2.38) into equation (2.35), we obtain the expression for the flow of current in the under damped circuit.

$$i(t) = -\left(\frac{V_0}{2j\beta L}\right)\left[e^{-(\alpha - j\beta)t} - e^{-(\alpha + j\beta)t}\right], \tag{2.39}$$

$$= -\frac{V_0}{\beta L}\left[\frac{(e^{j\beta t} - e^{-j\beta t})}{2j}\right] e^{-\alpha t} = -\frac{V_0}{\beta L} e^{-\alpha t} \sin \beta t. \tag{2.40}$$

The eigenfunction (2.40) of current is an exponentially decaying sinusoid with α the exponential decay constant and $\frac{V_0}{\beta L}$ the maximum amplitude of the current.

To investigate the current through the capacitor, we use the equations (2.24), (2.31) and (2.40) for critically damped, over damped and under damped oscillation, respectively. The plot of current through the circuit as a function of time for the different cases of damping as shown in Figures 2.2 and 2.3, are similar to the results obtained by Madhu [18].

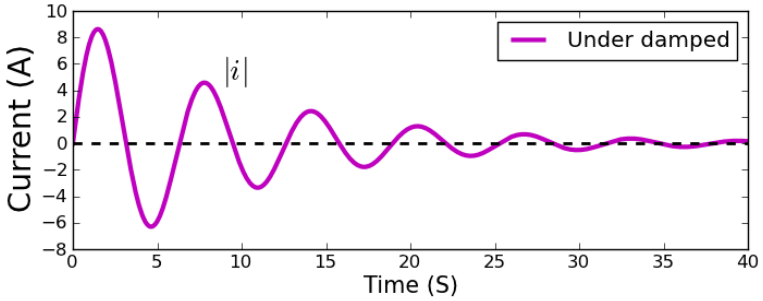

Figure 2.2. Current as a function of time for under damped oscillation, for $L = 1$ H, C $=$ 1 F and R $= 0.2\ \Omega$, $V_0 = 10$ V.

In the case of under damped oscillation Figure 2.2, the current is sinusoidal with decreasing amplitude. For the cases of critical damping and over damping Figure 2.3, current starts

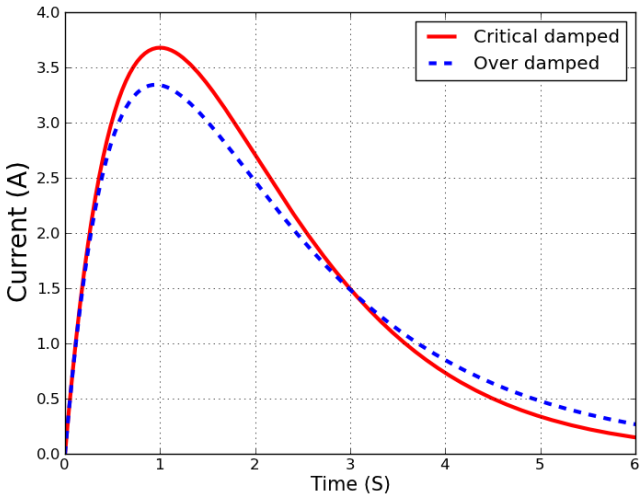

Figure 2.3. Current as a function of time for critical and over damped oscillation, for $L = 1$ H, C $= 1$ F and R $= 2, 2.3\ \Omega$, $V_0 = 10$ V.

from zero, reaches a maximum after which it decays to negligible values.

We then differentiate the equations (2.24), (2.31) and (2.40), to obtain

$$E_{\text{Critical}} \propto \frac{V_0}{L}\left(\frac{R}{2L}t - 1\right)e^{-\frac{R}{2L}t}, \tag{2.41}$$

$$E_{\text{Over}} \propto \frac{V_0}{L(n_2 - n_1)}\left(n_2 e^{n_2 t} - n_1 e^{n_1 t}\right) \text{ and,} \tag{2.42}$$

$$E_{\text{Under}} \propto \frac{V_0}{\beta L}\left[\alpha \sin \beta t - \beta \cos \beta t\right] e^{-\alpha t}, \text{ respectively.} \tag{2.43}$$

The expressions, proportional to the electric field [2] across the capacitor, for the different cases of damping, are plotted in Figures 2.4 and 2.5.

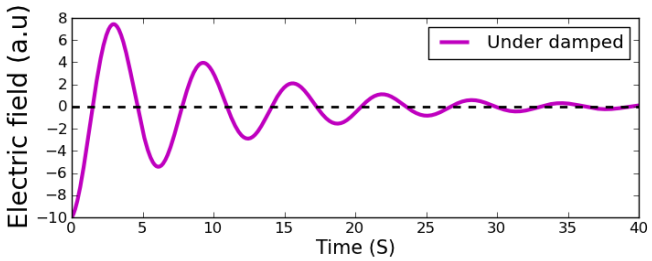

Figure 2.4. Electric field as a function of time for under damped oscillation , for $L = 1$ H, C $= 1$ F and R $= 0.2$ Ω.

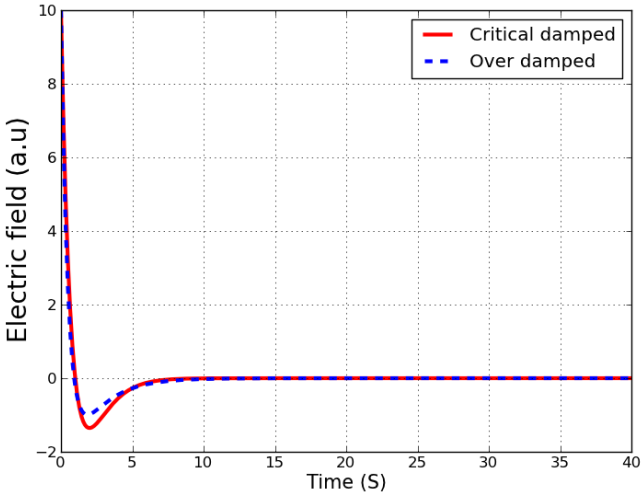

Figure 2.5. Electric field as a function of time for critical and over damped oscillation for $L = 1$ H, C $= 1$ F and R $= 2,\ 2.5$ Ω, respectively.

The mechanism of operation of the photoconductive antenna is complicated. We try to understand its operation by studying the RLC circuit for different damping cases so as to make a conclusion regarding which damping case best describes the operation of the antenna during THz emission and detection. Since the antenna we are using has GaAs as the photoconductive substrate and is operating at room temperature, the plasma oscillations involved are over damped [19]. Therefore, over damped oscillations best describe the operation of the antenna.

2.3 Fast Fourier Transforms

Fourier transformation is a mathematical method which uses integral calculus to transform a function of time into a function of frequency. This is sometimes referred to as transforming from time domain to frequency domain. The analytic function (the signal in time domain) is transformed by decomposing it using either Fourier sine/cosine or the complex Fourier transformation. The Fourier transform obtained corresponds to the frequency spectrum of the analytic function (i.e. source of the signal) and carries information of both the amplitude and phase of the signal. It is this information that we use to analyse all time dependant phenomenon in Chapter 5. However, in practical physics and engineering problems, such a closed mathematical formula does not always exist, instead, a set of experimental data constitutes the integrand [20]. In this respect, integration is performed mechanically or electronically using a suitable numerical scheme. In this case, the data to be transformed for example, data on waveform measurement of electric field through a material, is declared at the beginning and read into the programme as an "array" file. This depends on the programming language used. Then Fourier transforms are performed on the data using the Fourier transformation algorithm embedded in the software such as Python, the statistical software R, Matlab and Origin among others.

Fourier transformation has been applied in spectroscopy including infrared spectroscopy, nuclear magnetic resonance, optical spectroscopy, mass spectroscopy and electron spin spectroscopy among others [21, 22, 23]. The preferred algorithm here is the Fast Fourier Transform (FFT), because it is much faster and accurate (in the presence of rounding errors) than Discrete Fourier Transform (DFT) algorithms. It is utilised for most of the analysis in time domain spectroscopy.

Chapter 3

Generation and detection of THz radiation

3.1 Basic theory of THz as an electromagnetic wave

THz waves occupy a specific location in the electromagnetic spectrum, which makes them difficult to handle when compared to the waves adjacent to them [3]. In order to understand the interaction of THz waves with matter, for example macroscopically uniform media, we describe this relationship with Maxwell's equations [2], as it would be applied to any spectral region.

The macroscopic form of Maxwell's equations is given by

$$\nabla \cdot \mathbf{D} = \rho_f, \tag{3.1}$$

$$\nabla \cdot \mathbf{B} = 0, \tag{3.2}$$

$$\nabla \times \mathbf{E} = -\frac{\partial \mathbf{B}}{\partial t}, \tag{3.3}$$

$$\bigtriangledown \times \mathbf{H} = \mathbf{J}_f + \frac{\partial \mathbf{D}}{\partial t}, \tag{3.4}$$

where $\mathbf{E}$ is the electric field, $\mathbf{D}$ is the dielectric displacement, $\mathbf{H}$ is the magnetic field, $\mathbf{B}$ is the magnetic induction or magnetic flux density, ρ_f is the free charge density and $\mathbf{J}_f$ is the free current density [2]. These equations (3.1)-(3.4) together with the Lorentz force law

$$\mathbf{F} = q(\mathbf{E} + \mathbf{v} \times \mathbf{B}), \tag{3.5}$$

collectively form the basis of the theory of classical electrodynamics [2]. **D** and **H** are related to the fundamental fields **E** and **B** through a linear relationship given by

$$\mathbf{D} = \varepsilon_o \mathbf{E} + \mathbf{P} = \varepsilon \mathbf{E}, \tag{3.6}$$

$$\mathbf{H} = \frac{1}{\mu_0}\mathbf{B} - \mathbf{M} = \frac{1}{\mu}\mathbf{B}, \tag{3.7}$$

where ε_0 is permittivity of free space and has the value of approximately 8.854×10^{-12} (Fm^{-1}), and $\mu_0 (\simeq 1.257 \times 10^{-6})$ (Hm^{-1}) is the permeability of free space. The information about macroscopic-scale electromagnetic properties of matter is contained in the polarization **P** and the magnetization **M**. ε denotes the electric permittivity, and μ denotes the magnetic permeability. However, ε and μ are valid only if the medium is isotropic and linear [2]. The typical magnetic responses of matter are small, $|\mu - \mu_0| < 10^{-4}\mu_0$, and difficult to detect and analyse compared with their electric counterparts. This is mainly because of non-existence of magnetic monopoles in the electric field responses [2].

3.1.1 The wave equation

In this subsection, we use Maxwell's equations to derive a wave equation. We take the curl on both sides from equations (3.3) and (3.4), to obtain

$$\nabla \times (\nabla \times \mathbf{E}) = -\nabla \times \frac{\partial \mathbf{B}}{\partial t}, \tag{3.8}$$

$$\nabla \times (\nabla \times \mathbf{H}) = \nabla \times \mathbf{J}_f + \nabla \times \frac{\partial \mathbf{D}}{\partial t}. \tag{3.9}$$

We now substitute equation (3.7) into equation (3.8), to obtain

$$\nabla \times (\nabla \times \mathbf{E}) = -\mu \nabla \times \frac{\partial \mathbf{H}}{\partial t}, \text{ since } \mathbf{B} = \mu H. \tag{3.10}$$

Substituting equation (3.4) into equation (3.10), we obtain

$$\nabla \times (\nabla \times \mathbf{E}) = -\mu \left(\frac{\partial \mathbf{J}_f}{\partial t} + \frac{\partial^2 \mathbf{D}}{\partial t^2}\right). \tag{3.11}$$

At the same time substituting equation (3.6) into equation (3.11), we obtain

$$\nabla \times (\nabla \times \mathbf{E}) + \varepsilon\mu \frac{\partial^2 \mathbf{E}}{\partial t^2} = -\mu \frac{\partial \mathbf{J}_f}{\partial t}. \tag{3.12}$$

Using equation (3.3), the linear relations in equations (3.6) and (3.7), and equation (3.9), it can be shown that [2]

$$\nabla \times (\nabla \times \mathbf{H}) + \varepsilon\mu \frac{\partial^2 \mathbf{H}}{\partial t^2} = \nabla \times \mathbf{J}_f. \tag{3.13}$$

The auxiliary vector identity to be used is given by

$$\nabla \times (\nabla \times \mathbf{A}) = \nabla(\nabla \mathbf{A}) - \nabla^2 \mathbf{A}. \tag{3.14}$$

We apply the auxiliary vector identity, equation (3.14) into equation (3.12) and then use the linear relationship in equation (3.6), followed by equation (3.1), to obtain

$$\nabla^2 \mathbf{E} - \varepsilon\mu \frac{\partial^2 \mathbf{E}}{\partial t^2} = \mu \frac{\partial \mathbf{J}_f}{\partial t} + \frac{1}{\varepsilon} \nabla \rho_f. \tag{3.15}$$

In the similar way, we use equations (3.14) and (3.13), and the linear relations in equations (3.7) and (3.2) to obtain the relationship between magnetic field and free current density given by

$$\nabla^2 \mathbf{H} - \varepsilon\mu \frac{\partial^2 \mathbf{H}}{\partial t^2} = -\nabla \times \mathbf{J}_f. \tag{3.16}$$

We now assume that $\mathbf{J}_f$ is linear with $\mathbf{E}$,

$$\mathbf{J}_f = \sigma \mathbf{E}, \tag{3.17}$$

where σ is the electrical conductivity. Substituting $\nabla \rho_f = 0$ into equation (3.15) we obtain,

$$\nabla^2 \mathbf{E} = \sigma\mu \frac{\partial \mathbf{E}}{\partial t} + \varepsilon\mu \frac{\partial^2 \mathbf{E}}{\partial t^2}, \tag{3.18}$$

where the constants σ and ε are real and independent [2]. Now we substitute $\sigma = 0$ into equation (3.18), to obtain the wave equation for the case when the medium is an insulator or a dielectric material

$$\nabla^2 \mathbf{E} = \varepsilon\mu \frac{\partial^2 \mathbf{E}}{\partial t^2} = \frac{1}{v^2} \frac{\partial^2 \mathbf{E}}{\partial t^2}. \tag{3.19}$$

The electromagnetic waves propagate in homogeneous media at speed

$$v = \frac{1}{\sqrt{\varepsilon\mu}} = \frac{c}{n},$$

where $n = \sqrt{\frac{\varepsilon}{\varepsilon_0}}$ is the refractive index and $c = \frac{1}{\sqrt{\varepsilon_0 \mu_0}}$ is the speed of light in free space, assuming $\mu = \mu_0$. If we suppose a non-magnetic material, no conductive currents and negligible space charges, then [24]

$$\nabla \cdot \mathbf{D} = 0, \tag{3.20}$$

$$\nabla \times \mathbf{H} = \frac{\partial \mathbf{D}}{\partial t}. \tag{3.21}$$

Now using equation (3.3), the linear relation in equations (3.6), (3.7), (3.20), (3.21) and the auxiliary identity (3.14), we obtain the fundamental equation for generation and propagation of electromagnetic waves [25].

$$\nabla^2 \mathbf{E} - \frac{1}{c^2} \frac{\partial^2 \mathbf{E}}{\partial t^2} = \frac{\partial^2 \mathbf{P}}{\partial t^2}. \tag{3.22}$$

3.1.2 Transmission and reflection: Fresnel's equations

For the derivation of the formulae for transmission and reflection and analysis in this subsection, we have closely followed the references [2, 26, 27]. A wave encountering the interface between media with different refractive indices n_1 and n_2 will not only be refracted, but also be partly reflected. The ratio of the amplitude of the reflected wave to the incident wave is known as the amplitude reflection coefficient r. The ratio of the amplitude of the transmitted wave to the incident wave is known as the amplitude transmission coefficient t. The dependence of these coefficients on the angle of incidence θ_1, the angle of refraction θ_2 and polarization of the wave can be given by Fresnel's equation for an electromagnetic wave. In Figure 3.1, the reflected and refracted rays are shown for cases of plane polarization, when the electric field is;

1. in the plane of incidence.
2. perpendicular to the plane of incidence.

At the boundary; when the incident ray, reflected ray and refracted ray meet, there must be a match between the components of the electric field and magnetic fields on either side of the boundary.

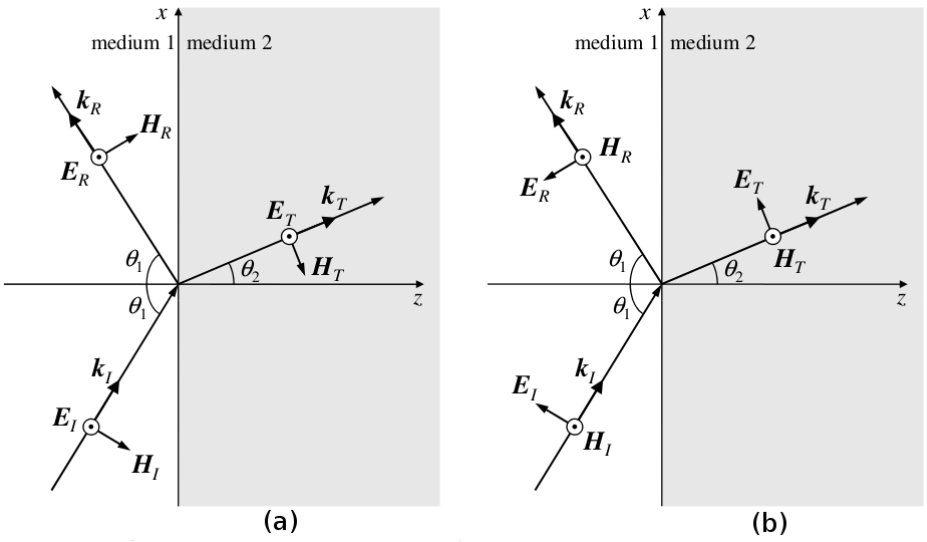

Figure 3.1. Reflection and transmission of incident wave (a) perpendicular, (b) parallel to the plane of incidence [2].

The subscripts $\parallel$ and $\perp$ refer to the orientation of the electric field vector; $\parallel$ for parallel to the plane of incidence and $\perp$, when perpendicular to the plane of incidence. These boundary conditions mean that the electric and magnetic fields must be the same on either side of the interface. From Figure 3.1(b), the surface component of the electric fields of the incident ray and transmitted ray are $\mathbf{E}_I \cos\theta_1$ and $\mathbf{E}_T \cos\theta_2$. The reflected ray being at an angle $(\pi - \theta_1)$, the surface component is $-\mathbf{E}_R \cos\theta_1$. Therefore, the first boundary condition is given by

$$\mathbf{E}_I \cos\theta_1 - \mathbf{E}_R \cos\theta_1 = \mathbf{E}_T \cos\theta_2. \tag{3.23}$$

In the case of polarization as indicated in Figure 3.1(b), the magnetic fields are parallel to the surface giving the second boundary condition

$$\mathbf{B}_I + \mathbf{B}_R = \mathbf{B}_T. \tag{3.24}$$

The magnitudes of $\mathbf{E}$ and $\mathbf{B}$ are related by

$$\mathbf{B} = \frac{n}{c}\mathbf{E}, \tag{3.25}$$

where n is the index of refraction and c the velocity of light. Substituting for $\mathbf{B}$ in equation (3.24), we obtain

$$n_1\mathbf{E}_I + n_1\mathbf{E}_R = n_2\mathbf{E}_T. \tag{3.26}$$

From equation (3.23)

$$\mathbf{E}_T = \frac{\mathbf{E}_I\cos\theta_1 - \mathbf{E}_R\cos\theta_1}{\cos\theta_2} \quad \text{and,} \tag{3.27}$$

from equation (3.26)

$$\mathbf{E}_T = \frac{n_1\mathbf{E}_I + n_1\mathbf{E}_R}{n_2}. \tag{3.28}$$

We now equate the two expressions for $\mathbf{E}_T$ to obtain

$$\frac{n_1\mathbf{E}_I + n_1\mathbf{E}_R}{n_2} = \frac{\mathbf{E}_I\cos\theta_1 - \mathbf{E}_R\cos\theta_1}{\cos\theta_2}. \tag{3.29}$$

Simplifying this expression we obtain the amplitude of reflection coefficient $r_\parallel$,

$$r_\parallel = \left(\frac{\mathbf{E}_R}{\mathbf{E}_I}\right)_\parallel = \frac{n_2\cos\theta_1 - n_1\cos\theta_2}{n_2\cos\theta_1 + n_1\cos\theta_2}. \tag{3.30}$$

Similarly, we evaluate the amplitude transmission coefficient when the electric field is parallel to the plane of incidence, as follows. From equations (3.23) and (3.26), we obtain expressions of $\mathbf{E}_R$,

$$\mathbf{E}_R = \frac{\mathbf{E}_I\cos\theta_1 - \mathbf{E}_T\cos\theta_2}{\cos\theta_1} \quad \text{and} \quad \mathbf{E}_R = \frac{n_2\mathbf{E}_T - n_1\mathbf{E}_I}{n_1}. \tag{3.31}$$

Equating the two expressions for $\mathbf{E}_R$, we obtain

$$n_2\mathbf{E}_T - n_1\mathbf{E}_I = \frac{n_1\mathbf{E}_I\cos\theta_1 - n_1\mathbf{E}_T\cos\theta_2}{\cos\theta_1}. \tag{3.32}$$

The expression for the amplitude transmission coefficient $t_\parallel$ is then given as

$$t_\parallel = \left(\frac{\mathbf{E}_T}{\mathbf{E}_I}\right)_\parallel = \frac{2n_1\cos\theta_1}{n_2\cos\theta_1 + n_1\cos\theta_2}. \tag{3.33}$$

We now obtain the amplitude reflection and transmission coefficient $r_\perp$, $t_\perp$ when the electric field is perpendicular to the plane of incidence, as indicated in Figure 3.1(a). The components of the magnetic field of the incident and transmitted rays parallel to the inter-

face are $\mathbf{B}_I \cos\theta_1$ and $\mathbf{B}_T \cos\theta_2$ respectively. The reflected ray being at an angle $(\pi - \theta_1)$, the normal component is $-\mathbf{B}_R \cos\theta_1$. The boundary condition is therefore given by

$$\mathbf{B}_I \cos\theta_1 - \mathbf{B}_R \cos\theta_1 = \mathbf{B}_T \cos\theta_2. \tag{3.34}$$

For the polarization shown in Figure 3.1(a), the electric fields are parallel to the interface giving a boundary condition

$$\mathbf{E}_I + \mathbf{E}_R = \mathbf{E}_T. \tag{3.35}$$

From equations (3.25) and (3.34), we obtain

$$n_1\mathbf{E}_I \cos\theta_1 - n_1\mathbf{E}_R \cos\theta_1 = n_2\mathbf{E}_T \cos\theta_2. \tag{3.36}$$

We evaluate the expression for $r\perp$ and $t_\perp$ by eliminating $\mathbf{E}_T$ and $\mathbf{E}_R$, respectively, from equations (3.35) and (3.36), and equating as follows;

$$r_\perp = \left(\frac{\mathbf{E}_R}{\mathbf{E}_I}\right)_\perp = \frac{n_1\cos\theta_1 - n_2\cos\theta_2}{n_1\cos\theta_1 + n_2\cos\theta_2}, \tag{3.37}$$

and

$$t_\perp = \left(\frac{\mathbf{E}_T}{\mathbf{E}_I}\right)_\perp = \frac{2n_1\cos\theta_1}{n_1\cos\theta_1 + n_2\cos\theta_2}. \tag{3.38}$$

Using Snell's law, $n_1 \sin\theta_1 = n_2 \sin\theta_2$, the amplitude reflection and transmission coefficients can be expressed in terms of angles θ_1 and θ_2 such that

$$r_\parallel = \frac{\tan(\theta_1 - \theta_2)}{\tan(\theta_1 + \theta_2)} \quad \text{and} \quad r_\perp = \frac{\sin(\theta_1 - \theta_2)}{\sin(\theta_1 + \theta_2)}, \tag{3.39}$$

$$t_\parallel = \frac{2\sin\theta_2\cos\theta_1}{\sin(\theta_1 + \theta_2)\cos(\theta_1 - \theta_2)} \quad \text{and} \quad t_\perp = \frac{2\sin\theta_2\cos\theta_1}{\sin(\theta_1 + \theta_2)}. \tag{3.40}$$

From the Figure 3.2, $r_\parallel$ goes through zero when $\theta_1 + \theta_2 = \frac{\pi}{2}$ and it changes sign which indicates phase reversal. The angle of incidence for which this occurs is known as the Brewster angle. The flow of energy across a surface, is known as irradiance[1]. Since irradiance is proportional to the square of the amplitude of reflection, we have the reflectance $R = r^2$,

[1]Irradiance is defined as "the power of an electromagnetic wave per unit area, and it is proportional to the square of the amplitude" [26].

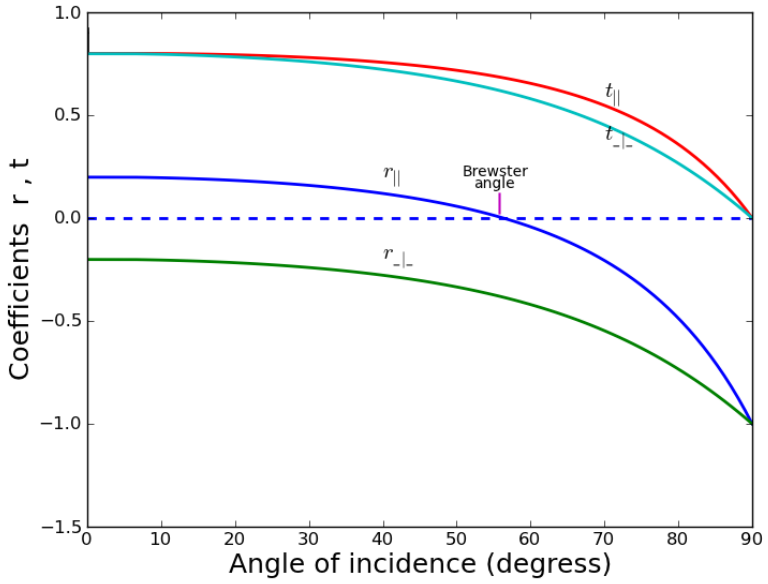

Figure 3.2. A plot of reflection (r) and transmission (t) coefficients, for the air/glass boundary with $n_2 = 1.5$, where $n_1 = 1$.

see Figure 3.3.

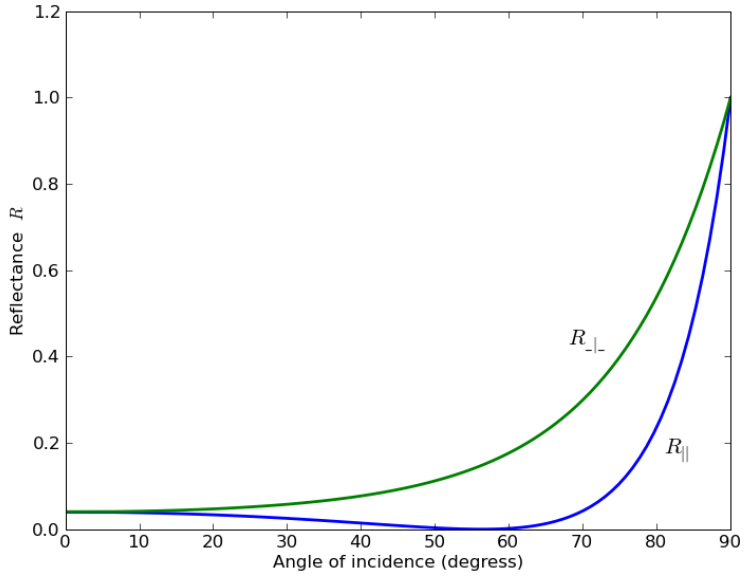

Figure 3.3. A plot of reflectance coefficient $R_{||}$, $R_{\perp}$ versus angle of incidence (degrees).

The transmittance T is the fraction of transmitted intensity and is given by

$$T = \frac{n_2}{n_1}\left(\frac{\cos\theta_1}{\cos\theta_2}\right)t^2. \tag{3.41}$$

Note that $R + T = 1$.

When the incident light is along the normal, the magnitudes of the reflection and transmission coefficients are independent of polarization since $(\cos\theta_1 = \cos\theta_2 = 1)$. These coefficients therefore become

$$r = r_{\parallel} = \frac{n_2 - n_1}{n_1 + n_2} = -r_{\perp}, \quad \text{and} \tag{3.42}$$

$$t = t_{\parallel} = \frac{2n_1}{n_1 + n_2} = t_{\perp} \quad \text{respectively.} \tag{3.43}$$

Using the same condition, the reflectance R and transmittance T are given by

$$R = r^2 = \left(\frac{n_2 - n_1}{n_2 + n_1}\right)^2, \quad \text{and} \tag{3.44}$$

$$T = \frac{n_2}{n_1}t^2 = \frac{4n_1n_2}{(n_1 + n_2)^2} \quad \text{respectively.} \tag{3.45}$$

3.2 Generation and detection of THz radiation

Various techniques have been used for the generation of THz radiation. These include; ultrafast switching in photoconductive antennas, rapid screening of the surface field via photoexitation of dense electron hole plasma in semiconductors, rectification of optical pulses in crystals, carrier tunnelling in a coupled double quantum well structure and coherent excitation of polar optical photons ([13], and the references therein).

Terahertz generation

THz technologies used in THz radiation generation are classified by the similarities in radiation characteristics and this includes broadband and continuous-wave (CW) sources. Using these two technologies terahertz can be (1) generated in nonlinear media (nonlinear crystals and diodes), and (2) radiated from accelerating electrons (for example from a

photoconductive antenna, electron accelerator and backward wave oscillator free-electron laser) [2]. This study focuses on pulsed THz generation using photoconductive antennas. However, this is not the only method for generating THz radiation, and a number of other techniques will now be briefly discussed.

3.2.1 THz generation from nonlinear optical media

THz radiation can be generated in nonlinear media from the incident electromagnetic wave via two nonlinear frequency conversions, frequency down and frequency up conversion. In the frequency down conversion, the second order nonlinear optical processes (optical rectification (OR) and difference frequency generation (DFG)) convert the incoming electromagnetic waves (femtosecond laser pulse and optical beat) utilizing a nonlinear crystal into their corresponding THz radiations (broadband pulsed and CW THz radiations) respectively.

In DFG an electromagnetic wave is produced at a frequency ω_T resulting from the interaction of two optical beams at different frequencies ω_1 and ω_2 with a non-linear crystal such that $\omega_T = \omega_1 - \omega_2$. The two laser beams with different frequencies form an optical beat through photomixing[2] which generates CW THz radiation [2].

Optical rectification on the other hand is almost similar to DFG but occurs within the broadband width of an ultrashort laser pulse. In general, during optical rectification, the radiation can be stimulated by one femtosecond laser pulse producing a broadband THz pulse. The broadband THz pulse generated from a femtosecond laser via this process has a broad spectrum (bandwidth of up to 10 THz) and has a shape resembling the optical pulse envelope.

3.2.2 Accelerating electrons THz sources

THz radiation can be generated from accelerating charge and time-varying currents. These are two different processes: photocurrent in semiconductors and free accelerating electrons

[2]Mixing two laser beams with different frequencies forms an optical beat, which generates CW THz radiation [2].

in vacuum. Each of these mechanisms can result in the generation of broadband or CW THz radiation.

3.2.2.1 Photocurrent in semiconductors

THz generation from photocurrent in semiconductors utilising a biased photoconductive antenna excited by laser beams. Two techniques utilising this process are summarised in Figure 3.4. In the first technique a femtosecond laser pulse produces broadband THz radiation by using transient photoconductive switching of the PC antenna. The other technique is referred to as photomixing, where two laser beams with different frequencies are mixed forming an optical beat which generates CW THz radiation at the beat frequency via a PC antenna. More information about the structure and operation of a PC antenna is given in Section 3.3.

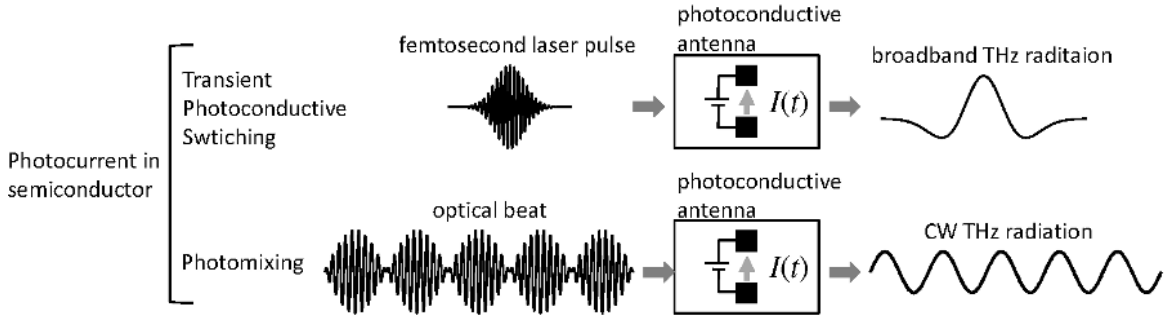

Figure 3.4. Source [2]: THz radiation from accelerating electrons by frequency down conversion.

3.2.2.2 THz generation from accelerating electrons in vacuum

The process of generation of THz radiation from free accelerating electrons based on frequency up conversion is summarised in Figure 3.5. In the process of frequency up conversion, THz radiation can be produced from accelerating electrons in vacuum using two basic mechanisms namely; relativistic electrons and electron accelerators. These mechanisms are influenced by the nature of the beam incident on the electron accelerators [2]. Using relativistic electrons (i.e electrons moving at a speed comparable to the speed of light), electron

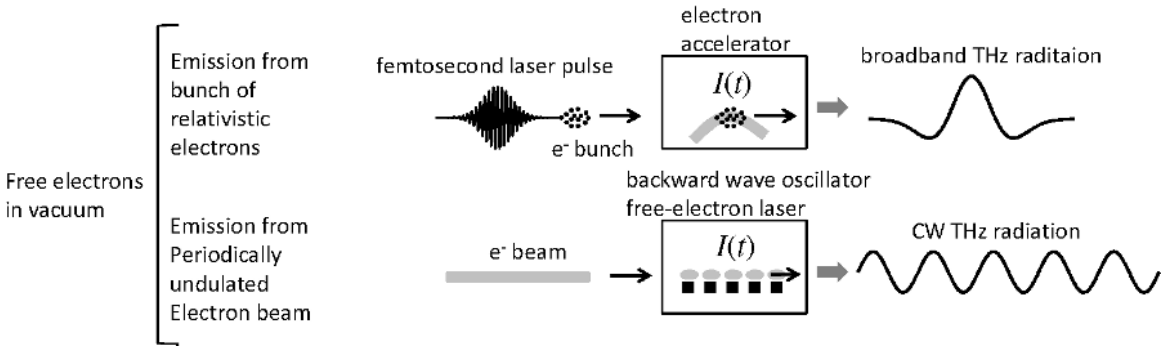

Figure 3.5. Source [2]: THz radiation from accelerating electrons by frequency up conversion.

accelerators produce extremely bright THz radiation. The process of generating the THz radiation from accelerating electrons results in both broadband and continuous wave THz radiation as indicated below;

1. Femtosecond laser pulse incident on the electron source, triggers the electron source, and sets in motion ultrashort pulses of electrons. The generated electrons are accelerated to relativistic speeds, smashing them into a metal target or forcing them into circular motion by a magnetic field. It is the acceleration of these transient electrons that generates coherent broadband THz radiation [2].

2. CW THz radiation can be generated using Backward Wave Oscillators (BWOs) and Free Electron Lasers (FELs). BWOs have a metal grating and are laboratory size equipment, while FELs consist of magnetic arrays and are small scale electron oscillators. Both mechanisms (BWOs and FEL) produce CW THz radiation [2].

3.3 Photoconductive (PC) antenna

A photoconductive antenna (PC) is an electrical switch which exploits the increase in electrical conductivity of semiconductors and insulators when they are exposed to light [2]. In the Figure 3.6 below, we show a labelled drawing of a photoconductive switch.

The PC antenna has a dipole antenna structure and is one of the most commonly used

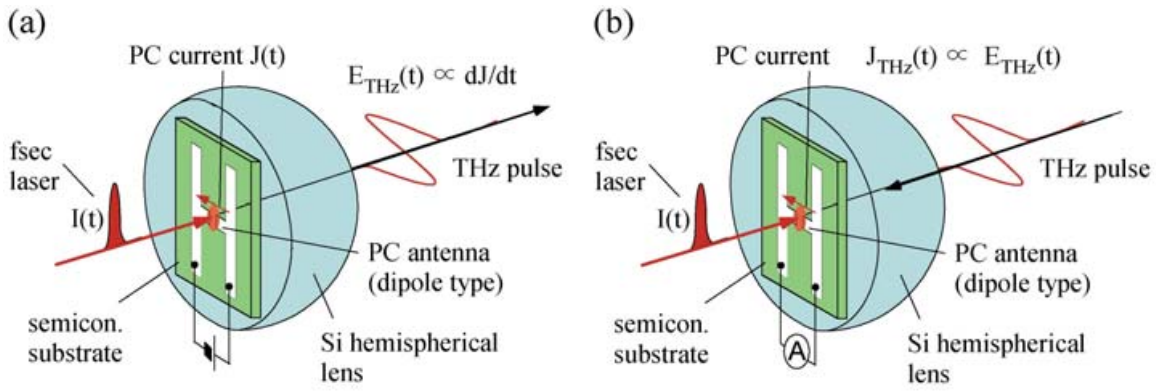

Figure 3.6. (a) A PC emitter antenna and (b) a PC detector antenna mounted on a hemispherical substrate lens [28].

emitters and detectors of THz radiation [29]. The THz radiation radiated from a classical dipole, has an angular frequency given by $\omega = \frac{1}{\sqrt{LC}}$. However, to produce radiation at terahertz frequencies, the values of capacitance C, and the inductance L must be very small (on the order of picofarad and picohenry). The PC antenna consists of two metal electrodes that are coated on a semi-insulating semiconductor substrate with a gap (PC gap) between the two electrodes [3]. The substrate being semi-insulating and enclosing the gap area, the electric energy is stored in this gap area [3]. The PC gap is biased with a dc voltage and illuminated with a femtosecond laser pulse which excites the PC gap, generating photo-excited charge carriers. These photo excited charge carriers are accelerated under the bias field ($E_b = \frac{V_b}{D}$, where V_b is the bias voltage and D the size of the PC gap) producing a photocurrent [30]. This transient current I_{PC} generates an ultra-short pulse of electromagnetic radiation (THz radiation). The relationship between the THz electric field amplitude and the photocurrent is given in equation (3.51).

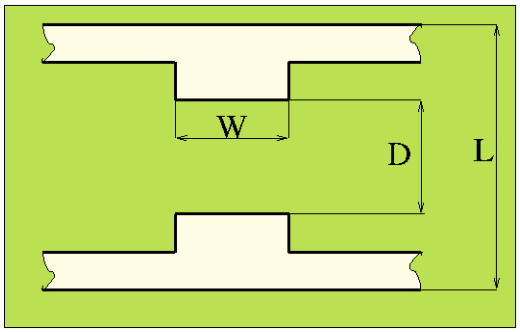

Figure 3.7. Geometrical parameters of the antenna

The gap area is a very important aspect of the a PC antenna since it is the active area with laser excitation and that is where THz wave generation and detection occurs in the PC antenna. The typical dimension of the PC gap D is $5-10$ μm, and the corresponding width W and antenna length L are $10-20$ and $30-50$ μm, respectively, for Hertzian dipole type antennas [30]. The geometrical parameters of a typical PC antenna are indicated in Figure 3.7. In our practical experimentation we use a PC antenna with the following dimensions, the PC gap D, of 10 μm, antenna width W, of 20 μm, and antenna length L, of 40 μm for the Photoconductive switch [31].

A typical PC switch Figure 3.8, has a bias voltage and a load resistor connected in series with a semiconductor. When laser light illuminates the PC antenna, the photons generate free electron carriers and holes [2]. However, for this laser light to generate photoinduced free carriers from the substrate, it must have enough photon energy, that means for generation to occur, the excitation optical pulse should have photon energy higher than the band gap of the substrate [3]. The increase in the number of free carriers and holes results

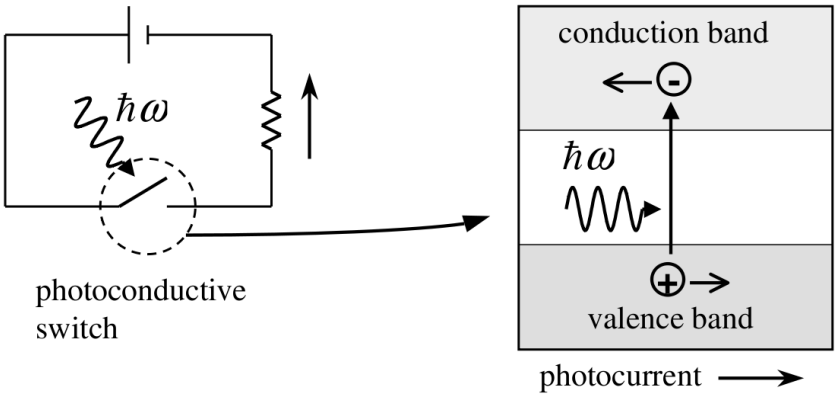

Figure 3.8. Photoconductive switch [2].

in the photoconductivity of the antenna [2].

In the generation and detection of THz radiation, the switching action of the PC antenna is vital, and should be in the subpicosecond time range. Low-temperature grown gallium arsenide (LT-GaAs) is most frequently used as a photoconductive material substrate for PC switches, because of its high mobility and short lifetime [2]. However, several other materials have also been tested, namely radiation-damaged silicon-on-sapphire (RD-SOS), chromium-doped gallium arsenide (Cr-GaAs), indium phosphide (InP) and amorphous

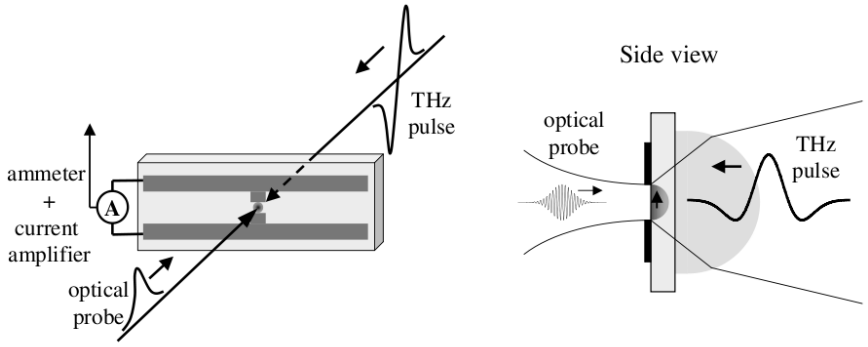

Figure 3.9. Schematic representation of THz pulse detection with a PC antenna [2].

silicon, as will be summarised in Subsubsection 3.4.1. Figure 3.9 shows the structure of a PC antenna excited by femtosecond laser.

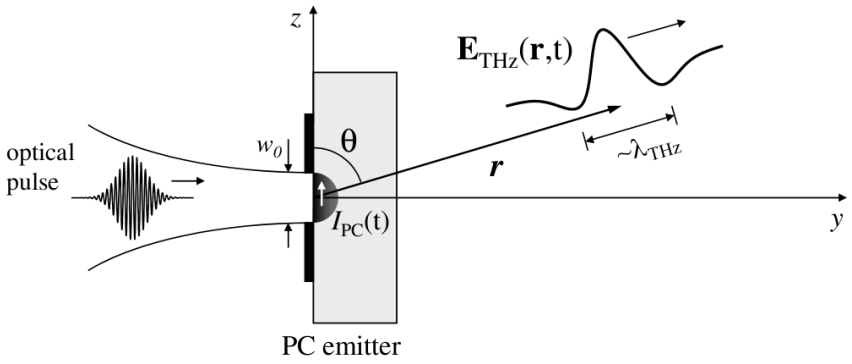

Figure 3.10. Electric dipole radiation from a PC antenna [2].

Figure 3.10 shows the electric dipole radiation from the PC antenna. To describe the properties of the radiation field, we use a dipole approximation. This approximation is valid because the size of the electron (source) used in emitting the radiation is much smaller (i.e comparable to the spot size of the optical beam $w_0 \approx 10\mu$m [2]) than the THz radiation wavelength.

In Figure 3.10 we assume dipole radiation in free space. The THz dipole radiation in free space [2] is given by

$$\mathbf{E}_{\mathrm{THz}}(t) = \frac{\mu_0}{4\pi}\frac{\sin\theta}{r}\frac{d^2}{dt^2}[p(t_r)]\hat{\theta}, \tag{3.46}$$

where μ_0 is the permeability of free space, and $p(t_r)$ is the dipole moment of the source at

the retarded time $t_r = t - \frac{r}{C}$. The time derivative of the dipole moment [2] is given by

$$\frac{d\mathbf{p}(t)}{dt} = \frac{d}{dt}\int \rho(\mathbf{r}^{'},t)\mathbf{r}^{'}d^3r' = \int \mathbf{r}^{'}\frac{\partial\rho}{\partial t}(\mathbf{r}^{'},t)d^3\mathbf{r}^{'}, \tag{3.47}$$

where $\rho(\mathbf{r}^{'},t)$ is the charge carrier density. The integral equation (3.47) can be simplified using the continuity equation given as

$$\nabla\cdot\mathbf{J} + \frac{\partial\rho}{\partial t} = 0, \tag{3.48}$$

where $\mathbf{J}(\mathbf{r}^{'},t)$ is the photocurrent density.

We now substitute equation (3.48) into equation (3.47), and then integrate by parts to obtain

$$\frac{d\mathbf{p}(t)}{dt} = -\int \mathbf{r}^{'}\nabla.\mathbf{J}(\mathbf{r}^{'},t)d^3\mathbf{r}^{'} = \int \mathbf{J}(\mathbf{r}^{'},t)d^3\mathbf{r}^{'}. \tag{3.49}$$

When we assume that the carrier transport is one dimensional, and then integrate from $-\frac{\omega_o}{2}$ to $\frac{\omega_o}{2}$, to obtain

$$\begin{aligned}\frac{d\mathbf{p}(t)}{dt} &= \int \mathbf{J}(\mathbf{r}^{'},t)d^3\mathbf{r}^{'} = \int_{-\frac{\omega_o}{2}}^{\frac{\omega_o}{2}} I_{PC}(\mathbf{r}^{'},t)dz^{'},\\ &= \omega_o I_{\mathrm{PC}}(t),\end{aligned} \tag{3.50}$$

where I_{PC} is the photocurrent and, ω_o is the spot size of the optical beam. We now substitute equation (3.50) into equation (3.46) to obtain,

$$\mathbf{E}_{\mathrm{THz}}(t) = \frac{\mu_0\omega_0}{4\pi}\frac{\sin\theta}{r}\frac{d}{dt_r}[I_{PC}(t_r)]\hat{\theta} \propto \frac{dI_{\mathrm{PC}}}{dt}. \tag{3.51}$$

The THz electric field is proportional to the time derivative of the photocurrent in the photoconductive gap of the antenna or the second derivative of the dipole moment [2]. The existence of E_{THz}, equation (3.51), indicates survival of the THz radiation in the far field, i.e at large distances from the PC emitter.

In the commonly used PC materials, e.g LT-GaAs, wave-material interactions are constituted of wave-free carrier interactions. However, during THz interaction with a conductor or semiconductor material, wave-free electron interactions are dominant. The interaction and transport of photoexcited electron-hole pairs can be described using the classical Drude-Lorentz model. This model is based on the following assumptions [3]:

1. individual carriers are independent of each other and no interaction occurs between them other than collisions,

2. the collision between carriers is instantaneous, and

3. the average interval between two collisions involving the same carrier is independent of the location or the carrier velocity.

However, the photocurrent in the PC antenna is time-dependent and is given as the convolution of the optical pulse envelope and the impulse response [2]

$$I_{\mathrm{PC}}(t) = \int I_{\mathrm{opt}}(t - t^{'})[en_c(t^{'})\nu(t^{'})]dt^{'}, \tag{3.52}$$

where $I_{\mathrm{opt}}(t)$ is the optical pulse intensity profile, $n_c(t)$ is the carrier density, e is the charge of the electron, and ν(t) is the average velocity of the electron [2].

The change in the carrier density due to impulsive excitation follows [2]

$$\frac{dn_c(t)}{dt} = -\frac{n_c(t)}{\tau_c} + \delta(t), \tag{3.53}$$

Solving the homogeneous part of equation (3.53), the dependence of $n_c(t)$ on time is given by

$$n_c(t) = \begin{cases} e^{-\frac{t}{\tau_c}} & \text{for} \quad t > 0, \\ 0 & \text{for} \quad t < 0, \end{cases} \tag{3.54}$$

where τ_c is the carrier lifetime, and δ(t) is Dirac delta function representing the impulsive optical excitation [2].

In the Drude-Lorentz model, the change in velocity of free carrier electrons is given by [2]

$$\frac{d\nu(t)}{dt} = -\frac{\nu(t)}{\tau_s} + \frac{e}{m}E_{DC}, \tag{3.55}$$

where τ_s is the momentum relaxation time, m is the effective mass of the carriers, and E_{DC} is the DC bias field. Let electron mobility be given as, $\mu_e = e\frac{\tau_s}{m}$, the inhomogeneous differential equation (3.55) can be solved using the integrating factor e^{t/τ_s} to obtain the

expression,

$$\nu(t) = \begin{cases} \mu_e E_{\mathrm{DC}}[1 - e^{-\frac{t}{\tau_s}}] & \text{for} \quad t > 0, \\ 0 & \text{for} \quad t < 0, \end{cases} \tag{3.56}$$

of the average velocity of free carrier electrons as a function of time.

We substitute equations (3.54) and (3.56) into equation (3.52), and suppose that the optical pulse is normally distributed (Gaussian) with pulse duration $2\sqrt{\ln 2} \cdot \tau_p$ (where τ_p is optical pulse duration) [2], to obtain

$$I_{\mathrm{PC}}(t) = \int_0^\infty I^0_{\mathrm{opt}} e^{-\frac{(t-t')^2}{\tau_p^2}} e^{\frac{-t'}{\tau_c}} \mu_e E_{DC} \left[1 - e^{-\frac{t'}{\tau_s}}\right] dt', \tag{3.57}$$

$$= \mu_e E_{\mathrm{DC}} I^0_{\mathrm{opt}} \int_0^\infty e^{-\frac{(t-t')^2}{\tau_p^2} - \frac{t'}{\tau_c}} \left[1 - e^{-\frac{t'}{\tau_s}}\right] dt'. \tag{3.58}$$

We integrate equation (3.58), to obtain

$$\begin{aligned} I_{\mathrm{PC}}(t) = \frac{\sqrt{\pi}}{2} \mu_e E_{DC} I^0_{opt} \Bigg[& \exp\left(\frac{\tau_p^2}{4\tau_c^2} - \frac{t}{\tau_c}\right) \cdot \mathrm{erfc}\left(\frac{\tau_p}{2\tau_c} - \frac{t}{\tau_p}\right) \\ & - \exp\left(\frac{\tau_p^2}{4\tau_{cs}^2} - \frac{t}{\tau_{cs}}\right) \cdot \mathrm{erfc}\left(\frac{\tau_{\mathrm{p}}^2}{4\tau_{\mathrm{cs}}^2} - \frac{\mathrm{t}}{\tau_{\mathrm{p}}}\right)\Bigg], \end{aligned} \tag{3.59}$$

where $\frac{1}{\tau_{cs}} = \frac{1}{\tau_c} + \frac{1}{\tau_s}$ and $\mathrm{erfc}(x) = 1 - \mathrm{erf}(x) = \frac{2}{\sqrt{\pi}} \int_x^\infty e^{-t^2} dt$.

Now differentiating equation (3.59), we obtain

$$\begin{aligned} \frac{dI_{pc}}{dt} = \frac{\sqrt{\pi}}{2} \mu_e E_{DC} I^0_{opt} \Bigg[& \frac{2\exp\left(-(\frac{\tau_p}{2\tau_c} - \frac{t}{\tau_p})^2 + \frac{\tau_p^2}{4\tau_c^2} - \frac{t}{\tau_c}\right)}{\sqrt{\pi}\tau_p} - \frac{\exp(\frac{\tau_p^2}{4\tau_c^2} - \frac{t}{\tau_c}) \cdot \mathrm{erfc}(\frac{\tau_p}{2\tau_c} - \frac{t}{\tau_p})}{\tau_c} \\ & + \frac{\exp\left(\frac{\tau_p^4}{4\tau_{cs}^2} \cdot \mathrm{erfc}(\frac{\tau_p^2}{2\tau_{cs}} - \frac{t}{\tau_p})\right)}{\tau_{cs}} - \frac{2\exp\left(-(\frac{\tau_p^2}{2\tau cs} - \frac{t}{\tau_p})^2 + \frac{\tau_p^4}{4\tau_{cs}} - \frac{t}{\tau_{cs}}\right)}{\sqrt{\pi}\tau_p} \Bigg], \end{aligned} \tag{3.60}$$

which is the differential equation describing the electric field in equation (3.51).

To investigate the photocurrent with time through the photoconductive (PC) antenna, we

use the equation (3.59), with the constants indicated in Table 3.1. The result is shown in

constant	numerical value used
m	6.097×10^{-31} Kg
e	1.60213×10^{-19} C
τ_s	3.0×10^{-14} s
τ_c	5.0×10^{-13} s
τ_p	4.8×10^{-14} s
τ_{cs}	$\tau_c\times\tau_s/(\tau_s+\tau_c)$
E_{DC}	1 [a.u.]
I^0_{opt}	1 [a.u.]

Table 3.1. Values of constants used in numerical simulations.

Figure 3.11. We then differentiate equation (3.60) to obtain the expression for the electric field as a function of time in a photoconductive antenna. The graphical representation of this is also shown in Figure 3.11.

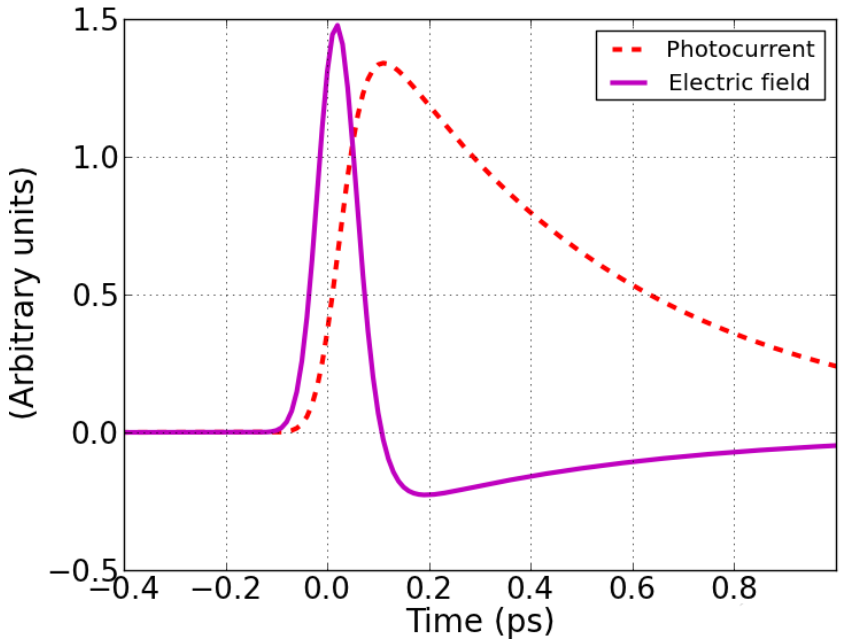

Figure 3.11. Photocurrent and electric field as a function of time.

3.4 Detection of THz pulse with a PC antenna

The mechanism for detecting THz radiation in the PC detector is similar to that of THz emission in the PC emitter. In general the detection process is perceived as an inverse process to the THz generation, with the main difference being that the emitter is connected to the bias voltage whereas the detector is connected to the current meter [32]. Since THz spectroscopy is an optical spectroscopy technique [2], the generation and detection processes use the same light source. In addition, the PC detector uses a coherent detection technique in that, it measures both the phase and amplitude of the electric field of the radiation. The detection technique is based on the pump-probe technique. In this technique, there is no absolute measurement of the time of the pump and probe. However, the time delay of the probe pulse relative to the pump pulse can be measured. Therefore, the time delay is used as the temporal reference frame [2, 32]. Ideally the detector is sensitive to the incoming THz field from the emitter for a short period of less than one picosecond [33]. The detection of the THz field is by the acceleration of the photocreated carriers by the incident THz field. The acceleration of the photocarriers is detected as current [32], and the profile (shape) of the THz field is mapped in time domain by measuring the current while varying the time delay [2, 33]. The detection of the THz electric field is in response to the photocurrent $J(t)$ which depends on the incident THz electric field, E_{THz} and the transient surface conductivity $\sigma_s(t)$. The relationship between $J(t)$, E_{THz} and $\sigma_s(t)$ is given by [2].

$$J(t) = \int_{-\infty}^{t} \sigma_s(t - t^{'}) E_{THz}(t^{'}) dt^{'}. \tag{3.61}$$

Therefore, since the surface conductivity is time dependent, the photocurrent in response to the THz electric field can not flow instantaneously [2]. Using the convolution theorem, the Fourier transform of (3.61), as shown by Lee [2], indicates that the carrier dynamics of the PC material limit the bandwidth of the PC receiver. Similar to the emitter, the carrier life time of the substrate in the detector limits the time resolution of the PC detector [32].

3.4.1 Materials for Photoconductive switches

A wide variety of materials have been used for the construction of photoconductive antennas. Some examples are shown in Table 3.2. Of all these materials, the most commonly

Photoconductive materials	Carrier lifetime (Ps)	Mobility ($cm^2/(V.s)$)	Resistivity (Ω.cm) (Breakdown field, V/cm)	Band gap (ev at R.T)
Cr:doped SI-GaAs	$50-100.0$	$\simeq 1000$	10^7	1.43
LT-GaAS	0.3	$150-200$	$10^6(5\times10^5)$	1.43
SI-InP	$50-100.0$	$\simeq 1000$	4×10^7	1.34
Ion-Implanted InP	$2-4.0$	200	$>10^6$	1.34
RD-SOS	0.6	30		1.10
Amorphous Si	$0.8-20.0$	1	10^7	1.10
MOCVD CdTe	0.5	180		1.49
LT-$In_{0.52}Al_{0.48}As$	0.4	5		1.45
Ion-Implanted Ge	0.6	100		0.66

Table 3.2. Characteristics of ultra fast photoconductive materials [32].

used materials for THz emitters and detectors are, radiation-damaged-silicon-on sapphire (RD-SOS) and low-temperature grown gallium arsenide (LT-GaAs) [2, 32]. RD-SOS is prepared by implanting argon, silicon or oxygen ions into SOS samples. Implanting results in dislocations that cause shortening of carrier life times [2]. Some of the desirable properties for photoconductive materials of high quality include short carrier life time, high carrier mobility and high breakdown voltage [2]. The properties of LT-GaAs, including carrier life time, depend mainly on the growth conditions and parameters used during molecular beam epitaxy (MBE) at lower substrate temperature ($\sim 200°C$) as well as the annealing process that follows after. GaAs has advantages in that it is highly transparent at THz frequencies, it has large nonlinear optical coefficients and a small mismatch between optical group velocity and THz phase velocity [2].

3.5 Laser spectroscopy in general

The basis of atomic and molecular physics experimentation is to gain information about the structure of atoms and molecules, and their mutual interaction. It also entails deter-

mination of bonding and ionization energies with the purpose of investigating electric and magnetic moments and their influence on the interaction energy [34]. To achieve these goals, various experimental techniques have been developed, of which one of the most powerful and accurate is spectroscopy.

3.6 General principles in the "pump-probe method"

In the pump-probe method, we need at least two individual sets of ultrashort light/laser pulses of comparable time duration. One of these goes through the sample at time $t = 0$, and this is called the "pump" pulse. The second one is delayed and it goes through the sample at time $t + \Delta t$. This time delay Δt, is as a result of an increased optical path traversed by the probe. This laser pulse is referred to as the "probe" pulse [35, 36]. To analyse the action of the pump on the sample, we use two different ways. These include:

(1) Time-resolved absorption technique; which involves comparing the modifications of the probe pulse characteristics after crossing the sample, before and after the action of the pump pulse.

(2) Observing new effects created by the probe itself before and after the action of the pump pulse (Raman scattering spectroscopy, laser induced fluorescence and coherent anti- stokes Raman spectroscopy (CARS), e.t.c).

3.7 THz time-domain spectroscopy

Terahertz time domain spectroscopy (THz-TDS) is a spectroscopic technique that uses THz pulsed radiation [30]. A typical THz-TDS system consists of an emitter of THz radiation, beam forming optics and a THz detector. The THz emitter is stimulated by femtosecond (fs) laser pulses. The beam forming optics consist of collimating and focusing lenses or mirrors, a sample holder and an optical delay line among others. The experimental setup for generation and detection of THz pulses which uses a fs laser is similar to the pump-probe technique [2]. A sketch of the typical setup of the experimental scheme is shown below, in Figure 3.12.

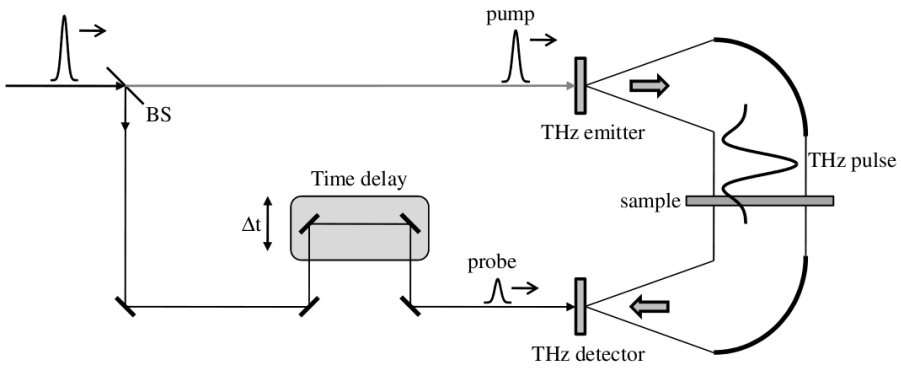

Figure 3.12. Shows a schematic diagram of a typical setup for generation and detection of THz pulses using femtosecond optical pulses [2].

In the experimental scheme, the beam splitter provides two synchronized pulses, the pump beam and the probe beam. The pump beam is used to generate the THz pulse by illuminating the emitter. The probe pulse goes to the detector and is used for sampling THz-induced transients and obtaining the pulse profile. THz pulses can be generated by transient currents in a photoconductive antenna or optical rectification in a nonlinear optical crystal. Similar to the generation process, detection of THz pulse can also be done using either a photoconductive antenna or a nonlinear crystal [2]. Note that the PC antenna is an electronic network and consists of a series RLC circuit with resistance R, capacitance C and inductance L. This electronic network is vital in describing the relationship between the induced current I_{THz} and the incident THz electric field [37]. In THz-TDS, we use a difference absorption spectroscopy technique where the THz pulse is measured with and without the sample [2]. The absorption and dispersion of the sample can be obtained by analysing the Fourier transformation of the THz radiation. This is due to the fact, that THz-TDS determines both the amplitude and the phase of the THz radiation [2]. The electric field of the THz pulse is measured as a function of time, $E(t)$ and transformed to frequency domain, $E(\omega)$.

Chapter 4

Experimental setup and methods

4.1 The general experimental setup

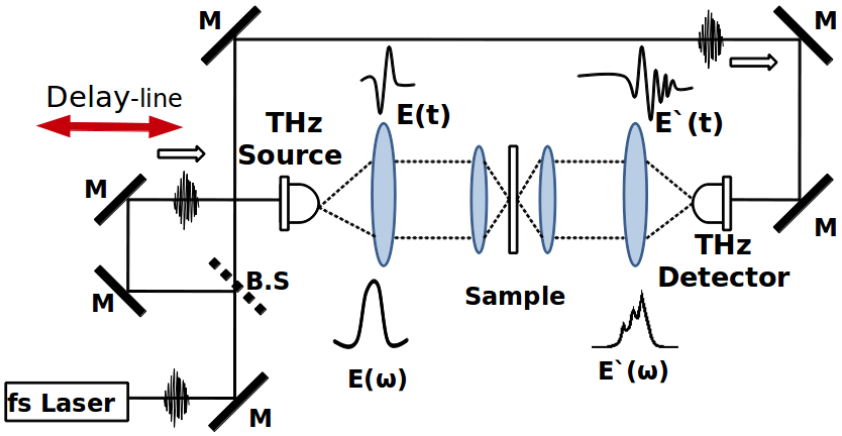

Figure 4.1. Experimental setup for generating and detecting THz radiation, **M**: Mirror, **B.S**: Beam Splitter.

The experimental setup for THz-TDS is shown in Figure 4.1. On the left side of the figure, a femtosecond laser (**fs laser**) produces an optical pulse train of femtosecond pulses. A femtosecond laser is necessary for short switching times, otherwise THz radiation will not be generated [2]. A beam splitter (**B.S**) provides two synchronized pulses, one going to the emitter and the other to the detector. The THz pulse created by the emitter (THz source) is collimated by the silicon lens [2]. The collimated pulse from the emitter, goes through several beam forming optics, passing through the sample, which absorbs some frequency

components. This changes the pulse shape, and the transmitted THz pulse passes to the detector. The second optical pulse gates the THz detector to measure the THz pulse as a function of time. By moving the delay, the time delay between the two pulses is changed, thus sampling the electric field of the THz pulse in a pump-probe gating scheme. The detector measures the electric field amplitude of the electromagnetic wave [14].

4.2 Information on Menlo Systems setup.

Figure 4.2 shows a sketch layout of Menlo Systems TERA K8 scientific-platform kit used as a THz spectrometer. It is this typical layout we used in our experiments. It consists of a femtosecomd (fs) laser as the source of fs pulses, a half wave plate, ($\lambda/2$) and a quarter wave plate ($\lambda/4$), THz detector (antenna), THz emitter (antenna), some mirrors used for photocurrent and THz signal adjustments and polarization beam splitter which splits the laser beam into the generation arm and the detection arm. The half wave plate ($\lambda/2$) can be used to set the power ratio between the generation beam and the detection beam.

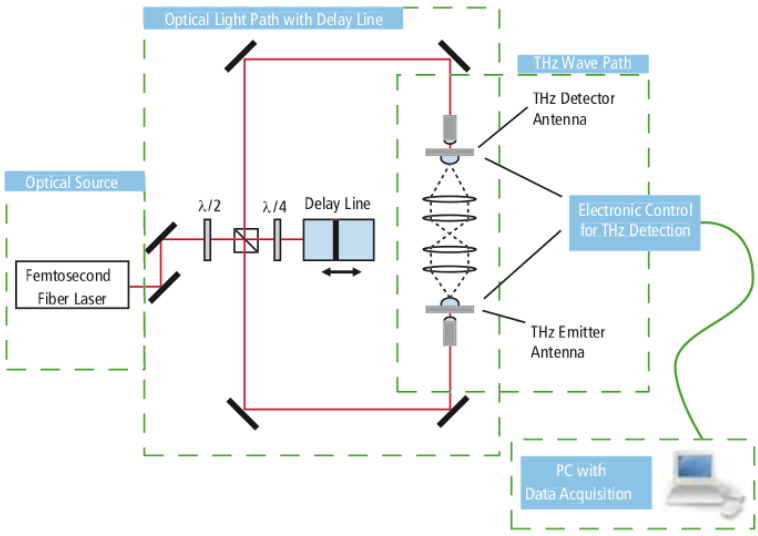

Figure 4.2. Sketch setup of the THz-TDS spectrometer [38].

The antenna used in our experimentation was a 20 μm Dipole antenna with antenna substrate LT-GaAs of dimension 5.0 $\times$ 5.0 mm^2. The photoconductive gap was of size 5 μm.

4.3 THz transparent materials

Optically transparent solid materials are important components of most optical devices and their characteristics are important for high-power application. Some of these materials are used as windows for laser, cryostats, optical cells, beam dividers etc, and as substrates for optical devices such as gratings and polarisers [39]. Glass is used as a universal window material since it is transparent in the whole visible range. However, standard glass can not serve the same purpose in the THz range since it is optically opaque for wavelengths longer than 3 μm, which corresponds to frequencies lower than 100 THz [39].

4.3.1 Optical properties of solids

The absorption and refraction of a medium can be described by a single quantity called the complex refractive index $\tilde{N}$. The complex refractive index is described by the equation

$$\tilde{N} = n + ik \tag{4.1}$$

The real part n of $\tilde{N}$, is the normal refractive index, and this determines the velocity of light through the medium. The imaginary part k of $\tilde{N}$ is the extinction coefficient and this determines the absorption coefficient. k is directly related to the absorption coefficient α of the medium. The relationship between α and k, is derived by considering the propagation of plane electromagnetic waves through the medium with complex refractive index. According to Beer's law [40], $\alpha_I = \frac{4\pi k}{\lambda}$, where λ is the free space wavelength. More detail about the derivation is given in [40].

Figure 4.3 shows the refractive index for Si and Ge which at a wavelength of 5μm are 3.4 and 4, respectively. These values are similar to the corresponding refractive indices for Ge and Si which are 4.0 and 3.41, respectively, in the THz range [2]. Therefore, windows made of these materials suffer from high reflection [41], when the radiation is moving from air to the material. However, silicon lenses serve an important purpose of collimating the beam, when attached as hemispherical lenses to the GaAs PC antenna as indicated in section 4.3.1. The absorption coefficient of Si and Ge as function of wavelength is shown in Figure 4.4.

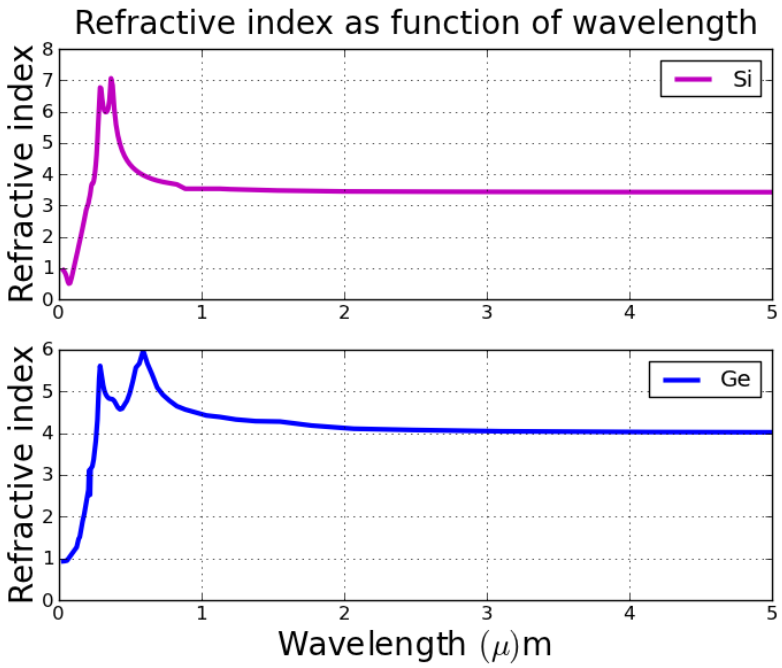

Figure 4.3. Refractive index of silicon and germanium as a function of wavelength, data of refractive indices and wavelengths is obtained from [42].

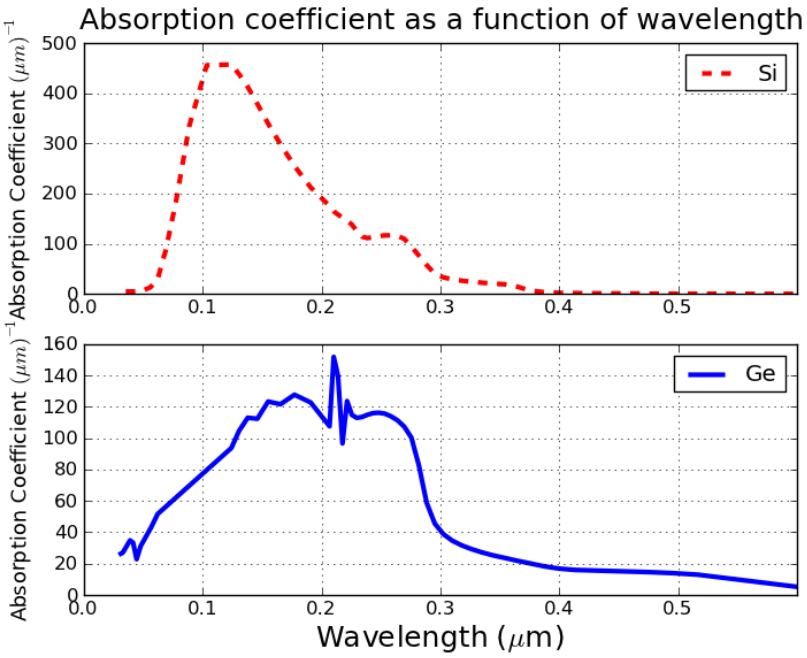

Figure 4.4. Absorption coefficient of silicon and germanium as a function of wavelength.

We use data for silicon and germanium obtained from [42] as an example to study the optical properties of solids. This data contains numerical values of photon energy E in electron volts (eV), the refractive index n, the extinction coefficient k and normal incidence reflection $R(\phi = 0)$. The photon energy E (eV) is converted to wavelength λ in μm by using the relationship $\lambda = \frac{1.2398}{E}$. To compute the dielectric function $\tilde{\varepsilon} = \varepsilon_1 + i\varepsilon_2$ from the complex index of refraction $\tilde{N} = n + ik$, use $\varepsilon_1 = n^2 - k^2$ and $\varepsilon_2 = 2nk$. The reflectance is given by

$$R = \frac{(n-1)^2 + k^2}{(n+1)^2 + k^2}. \tag{4.2}$$

This formula depends on both n and k. For the same thickness of material, silicon has a

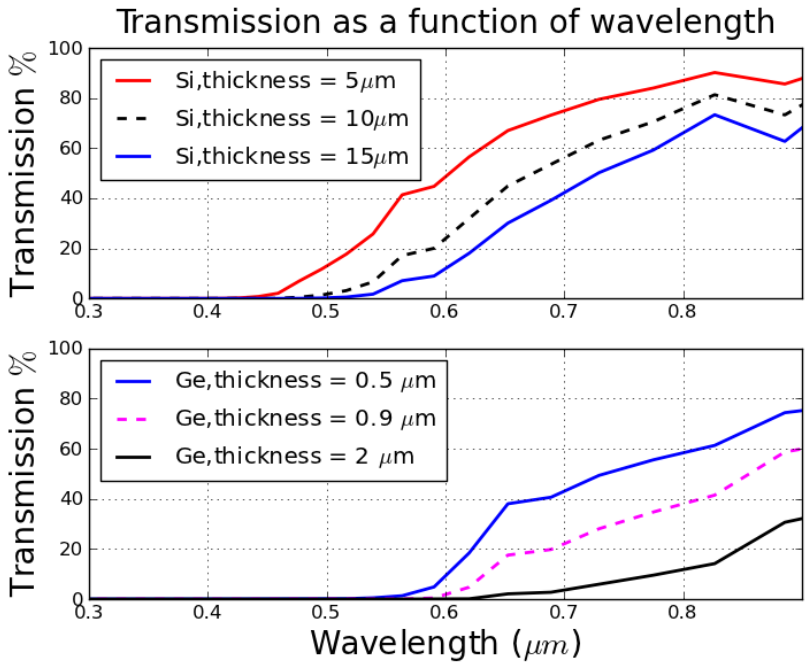

Figure 4.5. Transmission of silicon and germanium as a function of wavelength.

much higher transmission compared to germanium (in the visible range), Figure 4.5. Silicon is a suitable material for THz optics since it has low absorption and uniform refractive index ($n = 3.418$) in THz range [7]. Note that, this index of refraction is slightly lower than that of GaAs ($n = 3.595$). The refractive index of silicon being close to that of GaAs makes it a suitable material for the hemispherical silicon lens attached to the photoconductive emitter and detector to reduce the reflection of THz waves at the boundary of the emitter

and air.

4.3.2 Choice of THz transparent materials

Materials like pure fused silica and toxic arsenic trisulphide, have transmission limits of up to 5 μm and 12 μm, respectively. Some of the important solid window materials in the THz range are the simple two-atomic ionic crystals such as the alkali halides. Some crystalline materials such as alkali halides e.g. NaCl, LiF, CaF_2, BaF_2 and group II-VI compounds e.g. ZnS and ZnSe have reststrahlen[1] bands which limit their transmissivity for longer wavelength. These materials are useful as windows in the transparent spectral range between the two fundamental optical interactions namely, photon absorption at the low-frequency side and electron absorption at the electronic band edge [39]. Materials such as silicon and germanium are transparent from the mid-infrared to the microwave range except in a narrow band around 35μm [39]. Materials made from these substances are highly polarisable due to high polarisability of the covalent bonds of silicon and germanium and these materials are completely opaque in the visible range. Long wavelengths may be covered by polymers such as polystyrene, polyethylene (PE) or polytetrafluorethylene (Teflon). These two polymers are frequently used as substrates, windows and for making lenses in the long wavelength part of the terahertz regions [39]. However, some of these polymer (such as PE, Parylene, Teflon) have poor transparency in the THz range, which leads to high absorption loses [44]. In the same way, polymers become increasingly opaque at shorter wavelength [39]. Note that polymers are produced in different grades (e.g. high density and low density) which brings a difference in THz radiation transmissivity depending on the grade of crystallization, and the length of the free parts of the chains.

In our experimentation we use polymethylpentene (TPX) whose monomer is 4-methylpentene, to guide the THz radiation from the emitter to the detector. Figure 4.6 shows that TPX is transparent in both the ultraviolet and visible regions. TPX is also transparent in the whole THz range 30 μm - 300 μm [38]. In addition TPX can easily be shaped into lenses and beam splitters.

The refractive index of TPX is approximately constant at about 1.46 as indicated in Table

[1]The reststrahlen band is a high reflectance interval in the infrared wavelength region that is typical of crystals with at least partial ionic band [43].

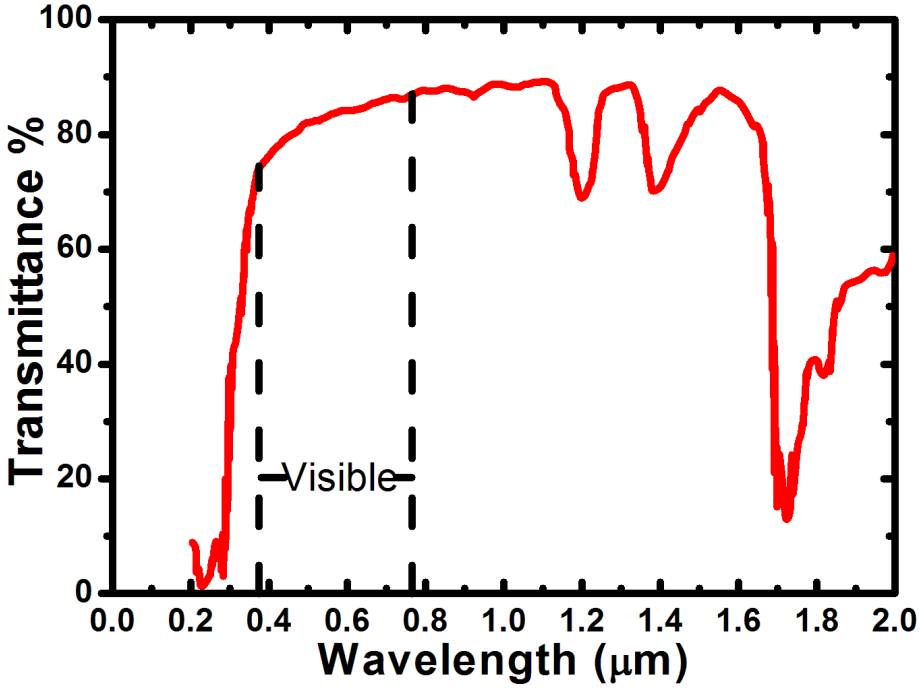

Figure 4.6. Transmission of TPX 2mm-thick sample. UV& VIS& NIR regions [38].

4.1.

λ (μm)	0.63	24	60	300	667	1000	3191
n	1.463	1.4568	1.4559	1.46	1.46	1.4650	1.466

Table 4.1. Shows the refractive index of TPX as function of wavelength [38].

Chapter 5

Results and discussion

5.1 The FFT on the voltage across a capacitor

In this section, we give some results on the application of FFT on voltage across a capacitor based on numerical simulations. To investigate the effect of FFT, we analyse the voltage across a capacitor as a function of time and the corresponding FFT in frequency domain for various values of resistance in an RLC circuit. Since the voltage across a capacitor in an RLC circuit oscillates, the different values of resistance R yield different types of damping. Damping reduces the amplitude of oscillations in an oscillatory system. In our analysis, we consider critical damping and under damping for different values of resistance R. In our investigation in this section, V_c represents the voltage across the capacitor in an RLC series circuit. To obtain V_c, we use the exact solution of the differential equation (2.9), and the relation in equation (2.5) to obtain V_c as a function of time given by

$$V_c = e^{\left(-\frac{R}{2L} \pm \sqrt{\left(\frac{R}{2L}\right)^2 - \frac{1}{LC}}\right)t}. \tag{5.1}$$

The numerical values of R, L and C used in the simulations are indicated in the respective subfigure captions.

Figure 5.1(a) shows the voltage across the capacitor in an RLC circuit series circuit with a small value of resistance ($R = 0.2\ \Omega$). The amplitude gradually decreases to zero (under damped oscillation). The FFT of this voltage shows that the output voltage has a bell shaped curve symmetrical about a particular (resonant) frequency, as shown in Figure

5.1(b). It is at the resonant frequency $\omega_0^{'}$ that the output voltage has the largest amplitude. The resonant frequency is related to capacitance and inductance by the relation [18]

$$\omega_0^{'} = \sqrt{\omega_0^2 - \left(\frac{R}{2L}\right)^2}. \tag{5.2}$$

When the resistance R is increased, the symmetry of the FFT disappears and the curve becomes positively skewed (skewed to the right).

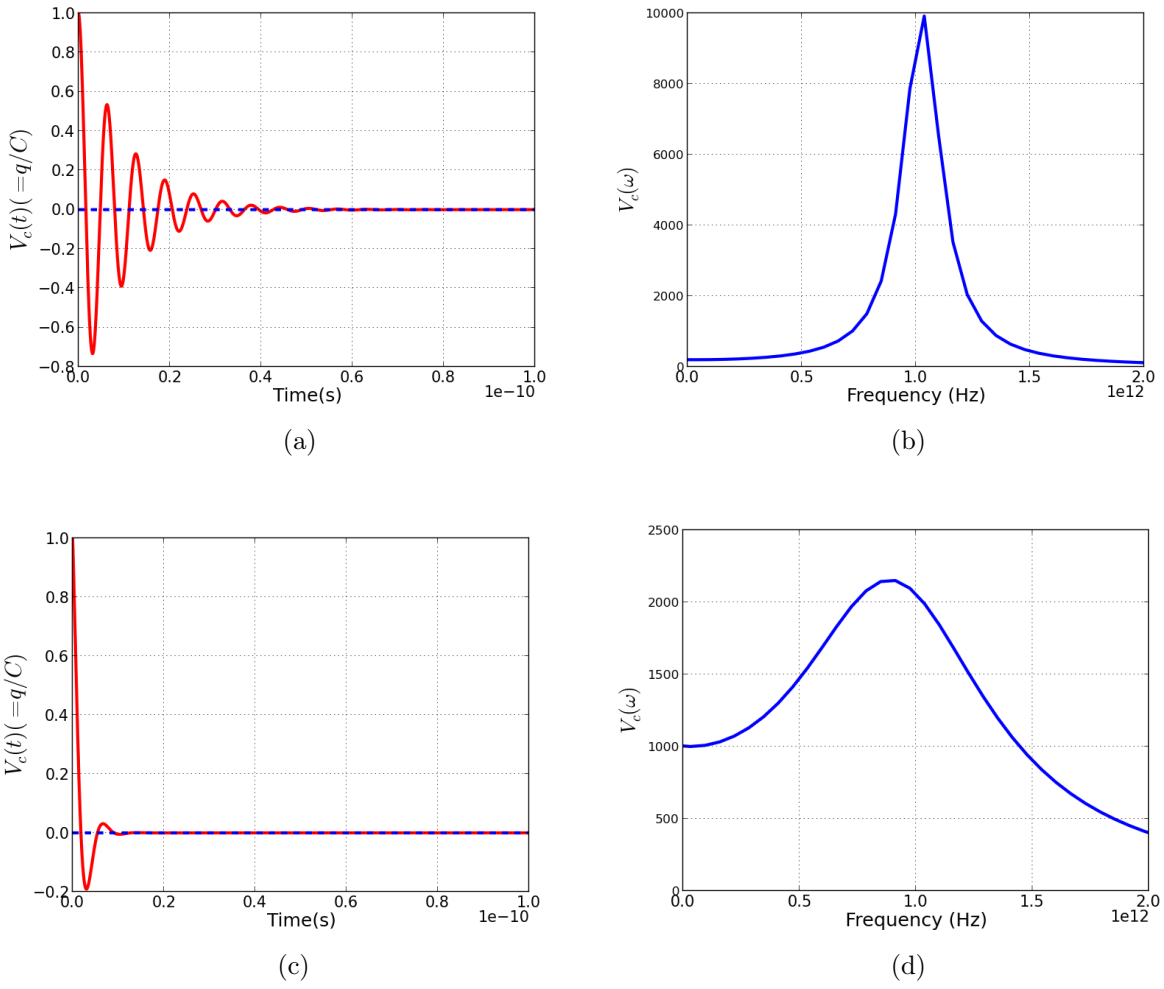

Figure 5.1. (a) and (c) show the voltage (V_c) as a function of time for $R = 0.2\ \Omega$ and $R = 1\ \Omega$, respectively, (b) and (d) are their corresponding FFT in frequency domain. For both cases $L = 10^{-12}$H and $C = 10^{-12}$F.

In general, we note that as the resistance increases, damping in the circuit changes from

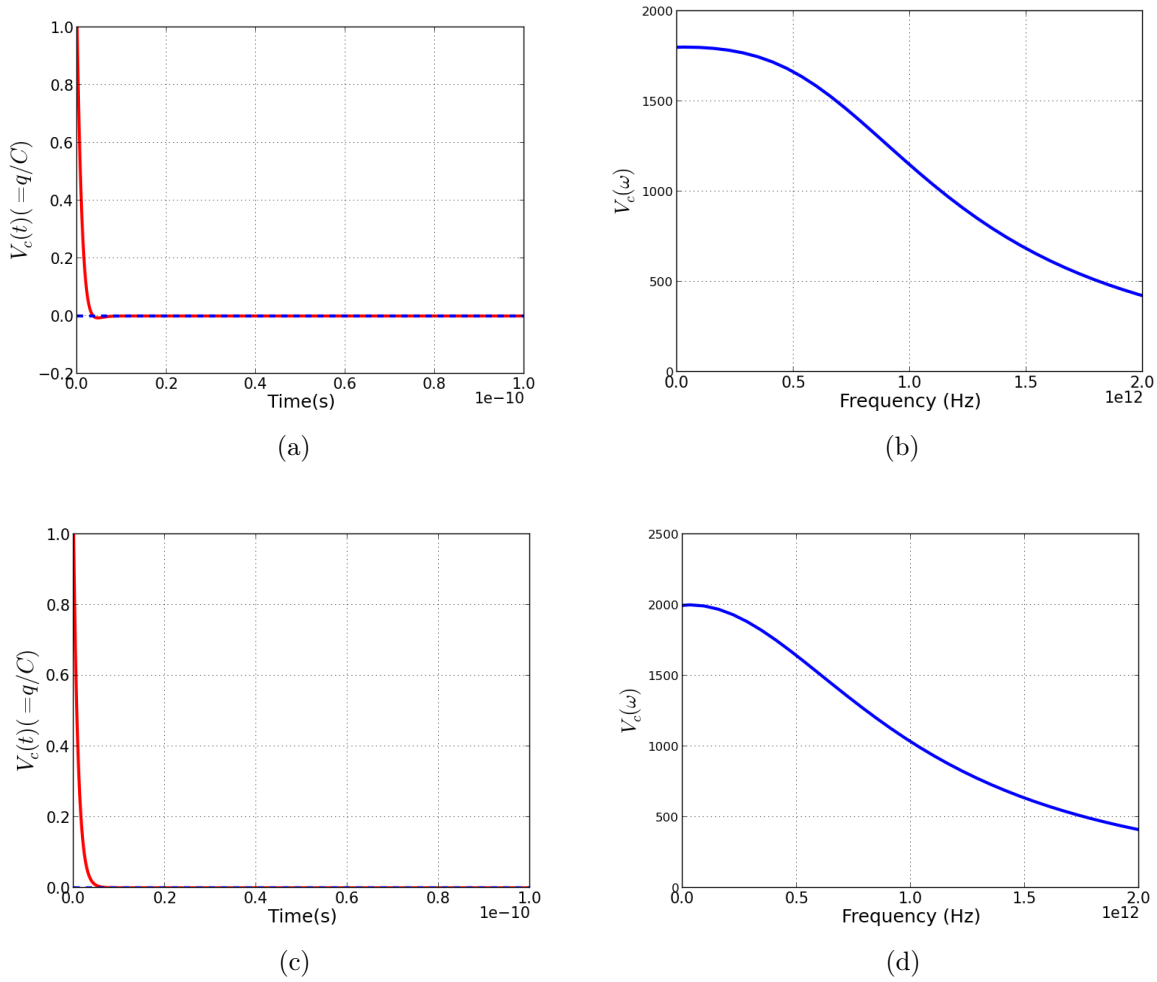

Figure 5.2. (a) and (c) show the voltage (V_c) as a function of time for $R = 1.8\ \Omega$ and $R = 2\ \Omega$, respectively, (b) and (d) are their corresponding FFT in frequency domain. For both cases $L = 10^{-12}$H and $C = 10^{-12}$F.

under damped oscillation (oscillation with decaying amplitude), to critical and then over damped oscillation where the voltage decays exponentially, see Figures 5.1 and 5.2. The simulations in Figures 5.1(b), 5.1(d), 5.2(b) and 5.2(d) convey information about bandwidth in the series RLC circuit. In a resonating series circuit, bandwidth measures the frequency selectivity (resonant frequency) of the circuit. It is given as the difference between two half-power frequencies [18]. In our case we consider the relationship of bandwidth as a function of resistance, given by bandwidth $= \frac{\mathrm{R}}{2\pi \mathrm{L}}$ [18], where R, L are the resistance and inductance, respectively. We note from our results that bandwidth increases with

resistance.

5.1.1 Absorption of radiation by materials

To investigate the absorptive properties of a material, we simulate this process using voltage across a capacitor from equation (5.1). We use the theory of RLC circuits to investigate the behaviour of THz pulses through an absorbing medium. Using equations (2.2) and (2.5), the current passing through a capacitor is given by

$$i = C\frac{dV_c}{dt}. \tag{5.3}$$

From equation (3.51), the electric field of the THz radiation E_{THz}, is proportional to $\frac{di}{dt}$ implying that

$$E_{\text{THz}} \propto \frac{d^2V_c}{dt^2}. \tag{5.4}$$

We use equation (5.4) to study the electric field across a capacitor before and after radiation passes through the substrate. In our simulation process, we multiply the generated voltage values by a transfer function T containing a periodic structure of alternating absorption and transmission bands. For example using $T = 0.9$ means that 90% of the radiation is transmitted and 10% is a absorbed in the absorption bands of the transfer function. In the complete transmission bands of the transfer function, all the radiation is transmitted. In Figures 5.3(a)-5.5(b), the top graphs (on the left) show V_c in frequency domain and their corresponding inverse Fourier transform in time domain (on the right). Since the $V_c(t)$ we are using is a real signal, by FFT we obtain a symmetrical waveform (around $\omega = 0$) with peaks at $\pm\omega_0^{'}$. The bottom graphs show V'_c (V_c multiplied by the transfer functions) and their corresponding inverse FFT (in time domain). Figures 5.6(a), 5.6(b) and 5.7, show $V_{c\ \text{diff}}(t)$, where $V_{c\ \text{diff}}(t) = V_c(t) - V_c^{'}(t)$ for different transfer functions T = 0.0, 0.5 and 0.9, respectively.

For a medium with high absorption, dips are observed at the absorption bands for $V_c^{'}(t)$ compared to the normal signal $V_c(t)$ in both frequency and time domains. A typical example of such a behaviour is observed in our simulation results in Figure 5.3(b). For a material with high transmission, the dips decrease and the signal approximates that of a non

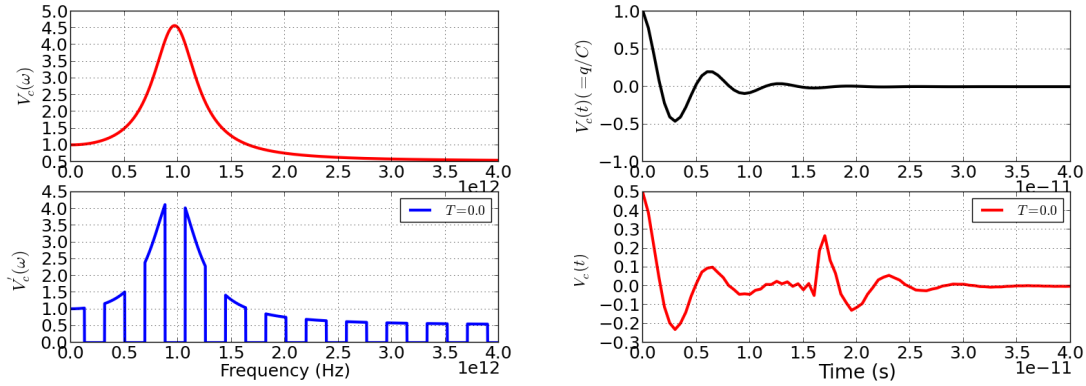

(a) (b)

Figure 5.3. (a) Voltage (V_c) as a function of frequency, (b) the corresponding inverse FFT, for $R = 0.5\ \Omega$, $L = 10^{-12}$H, $C = 10^{-12}$F and T = 0.0.

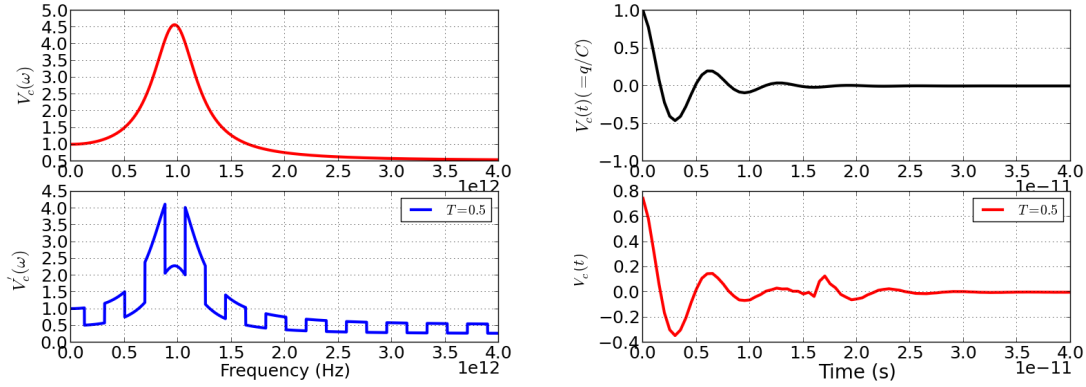

(a) (b)

Figure 5.4. (a) Voltage (V_c) as a function of frequency, (b) the corresponding inverse FFT, for $R = 0.5\ \Omega$, $L = 10^{-12}$H, $C = 10^{-12}$F and T = 0.5.

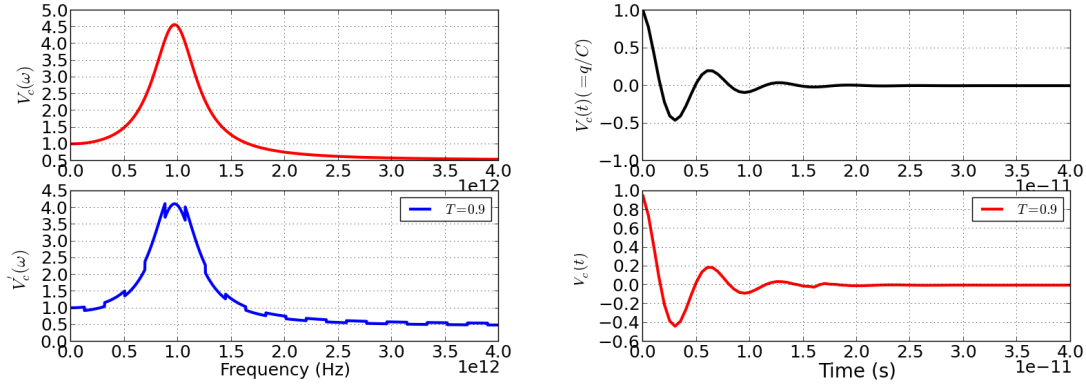

(a) (b)

Figure 5.5. (a) Voltage (V_c) as a function of frequency, (b) the corresponding inverse FFT, for $R = 0.5\ \Omega$, $L = 10^{-12}$H, $C = 10^{-12}$F and T = 0.9.

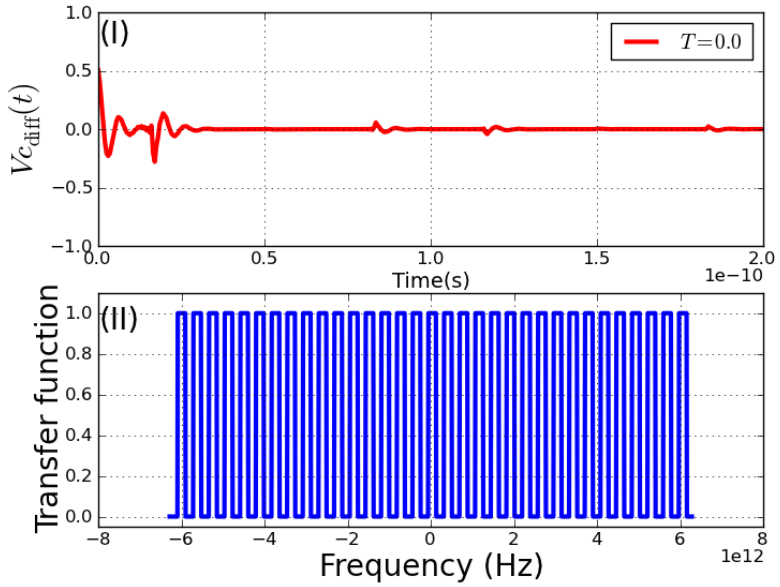

(a)

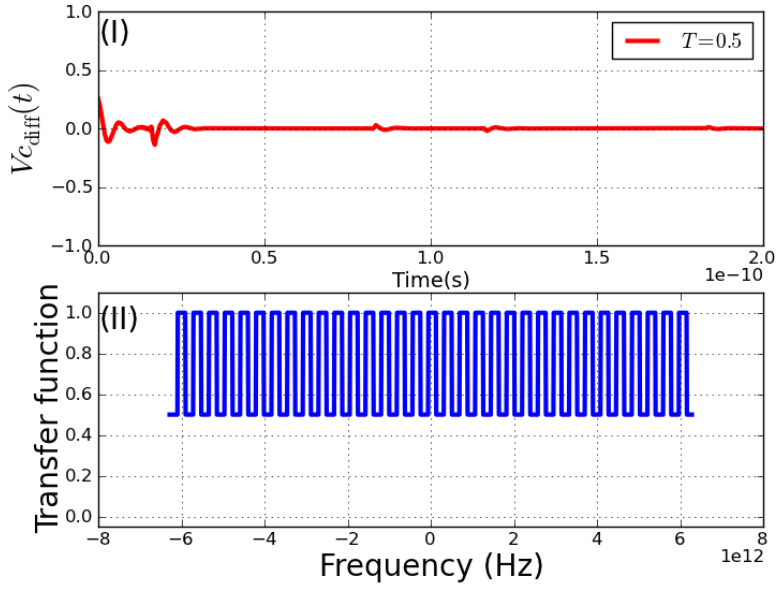

(b)

Figure 5.6. Shows $V_{c\ \mathrm{diff}}(t)$ as a function of time and the transfer function as a function of frequency for (a) T = 0.0 and (b) T = 0.5.

absorbing material, as shown in Figure 5.5(b). When the medium is strongly absorbing, the

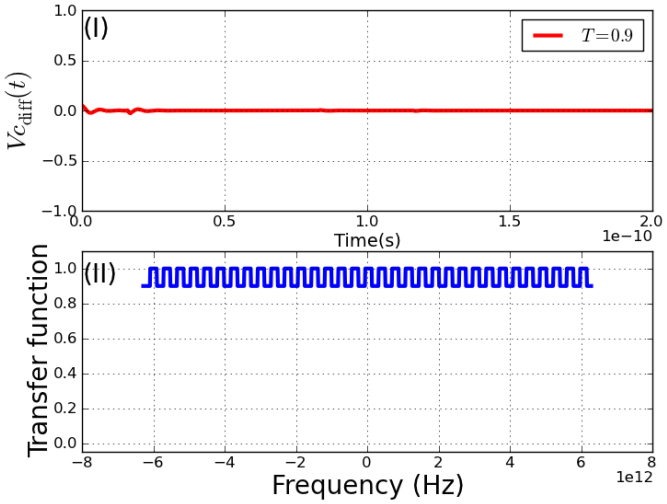

Figure 5.7. (I) $V_{c\ \mathrm{diff}}(t)$ as a function of time and (II) the transfer function as a function of frequency, for T = 0.9.

difference between the normal signal $V_c(t)$ and the signal through the absorbing material $V_c^{'}(t)$ is big, with dips still observed at the absorption bands, see Figure 5.6(a). When the absorption of the radiation by the material is low, the difference between $V_c(t)$ and $V_c^{'}(t)$ will be small. This trend can be observed by comparing our simulated results shown in Figure 5.6(a), 5.6(b) and 5.7.

Note that from the expression of V_c in equation (5.1) and the relation for electric field (5.4), the electric field measurement can be given by $E_{THz} = A^2 V_c$, where A is a constant. To emulate a transmission medium, we simulate the electric field using the transfer function T and the resultant electric field is given by $E_{THz}^{'} = E_{THz} \times T$. The results of our simulation are indicated in Figure 5.8, 5.9 and 5.10.

Similar to the voltage across a capacitor, the electric field of the THz pulse shows dips in the signal for a strongly absorbing medium at the absorption bands, Figure 5.8(b). The dips are negligible in the case of a medium with negligible absorption for the radiation. The depressions in Figures 5.8(a), 5.9(a) and 5.10(a) correspond to sharp absorption of the radiation at the corresponding frequencies.

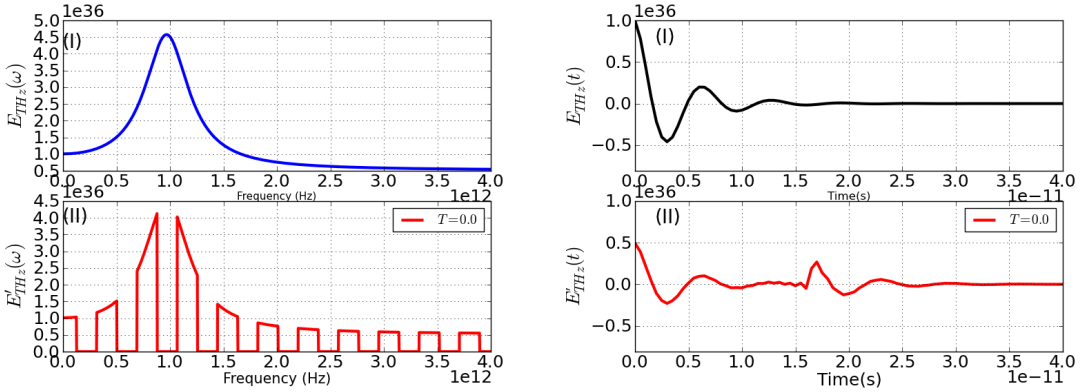

(a) (b)

Figure 5.8. (a) $E_{\mathrm{THz}} = \frac{dI(\omega)}{dt}$ as a function of frequency, (b) the corresponding inverse FFT of the electric field against time, for $R = 0.5\ \Omega$, $L = 10^{-12}$H, $C = 10^{-12}$F, and T = 0.0.

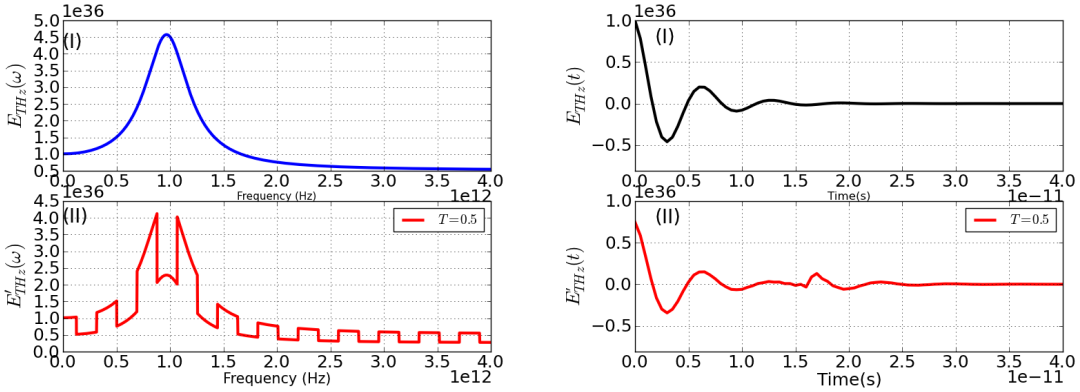

(a) (b)

Figure 5.9. (a) $E_{\mathrm{THz}} = \frac{dI(\omega)}{dt}$ as a function of frequency, (b) the corresponding inverse FFT of the electric field against time, for $R = 0.5\ \Omega$, $L = 10^{-12}$H, $C = 10^{-12}$F, and T = 0.5.

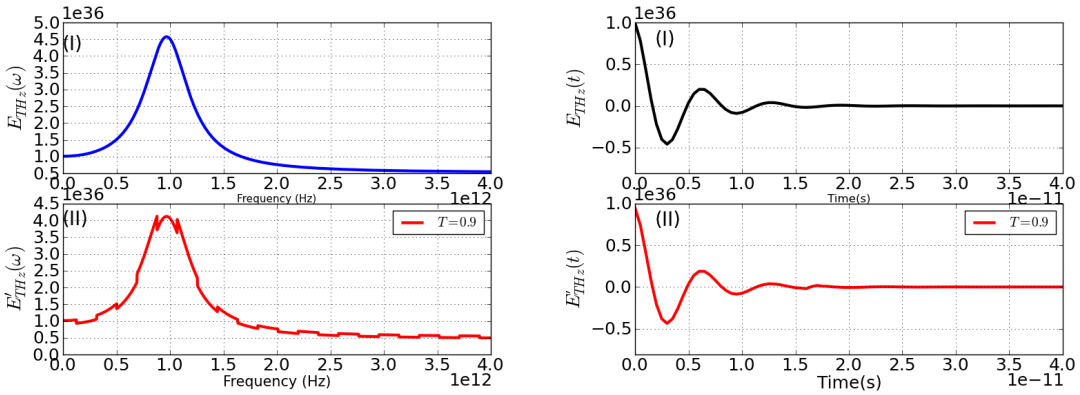

(a) (b)

Figure 5.10. (a) $E_{\mathrm{THz}} = \frac{dI(\omega)}{dt}$ as a function of frequency, (b) the corresponding inverse FFT of the electric field against time, for $R = 0.5\ \Omega$, $L = 10^{-12}$H, $C = 10^{-12}$F, and T = 0.9.

5.2 Transmission of a THz pulse through selected materials

5.2.1 Simulation of water vapour absorption measurement

We obtained the electric field absorption data of water vapour in the frequency domain from Lee [2], for the spectral range, 0.4 – 2 THz. The plot of this absorption data is shown in Figure 5.11. We then estimate the electric field transmission (Relative electric field transmission = 1 – Relative electric field absorption) through water vapour for the range 0.4 – 2 THz, as shown in Figure 5.12, using this data to theoretically produce the waveform of a THz pulse that has propagated through water vapour.

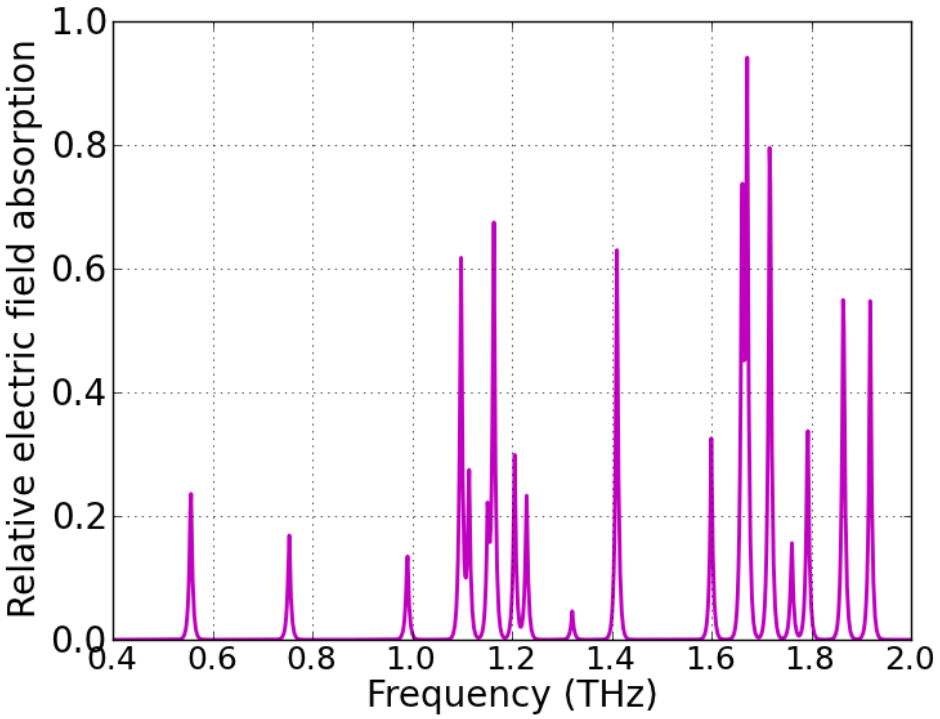

Figure 5.11. The absorption spectrum of water vapour from 0.4 – 2 THz.

Figure 5.13 shows the FFT of the electric field of the PC-antenna (without any absorption) as a function of frequency. It is calculated by taking the FFT of equation (3.60), describing the electric field of the PC antenna. Figure 5.14 shows the electric field intensity (square of E_{THz}) as a function of time. We observe that the electric field is symmetrical about the

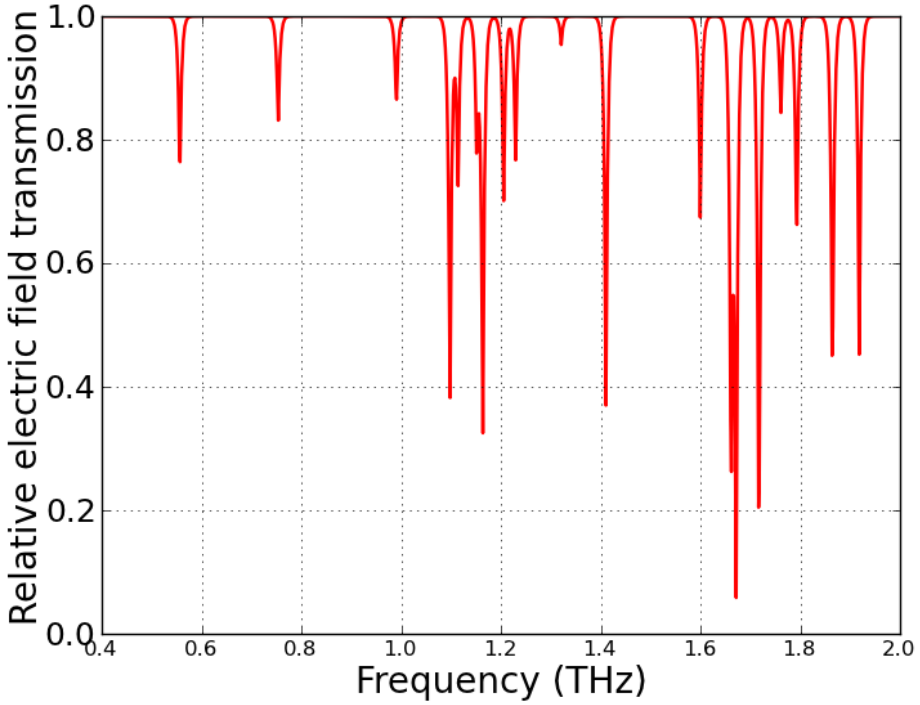

Figure 5.12. The transmission spectrum through water vapour from $0.4 - 2$ THz.

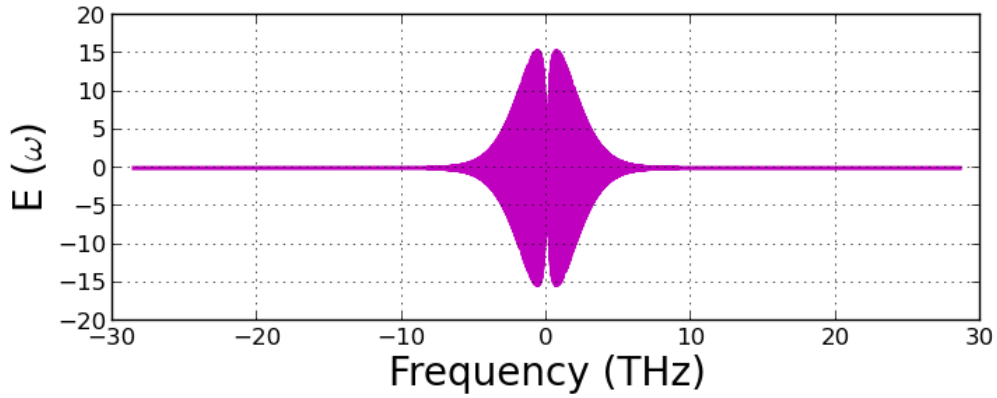

Figure 5.13. The electric field radiated by a PC antenna as a function of frequency, for values as indicated in Table 3.1.

origin. Using the absorption of water vapour indicated in Figure 5.11, we can interpolate this data to obtain the transmission through water for negative frequencies. We then, plot the original and interpolated transmission values on the same figure, as shown in Figure 5.15.

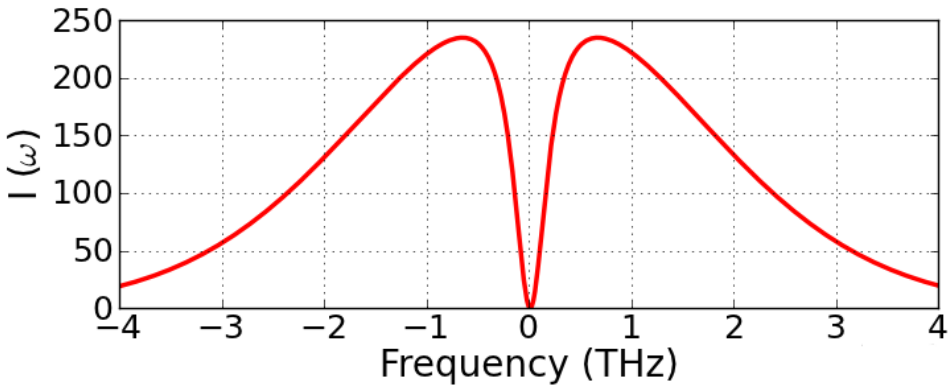

Figure 5.14. Intensity as a function of frequency, calculated as the square of $E(\omega)$, in Figure 5.13.

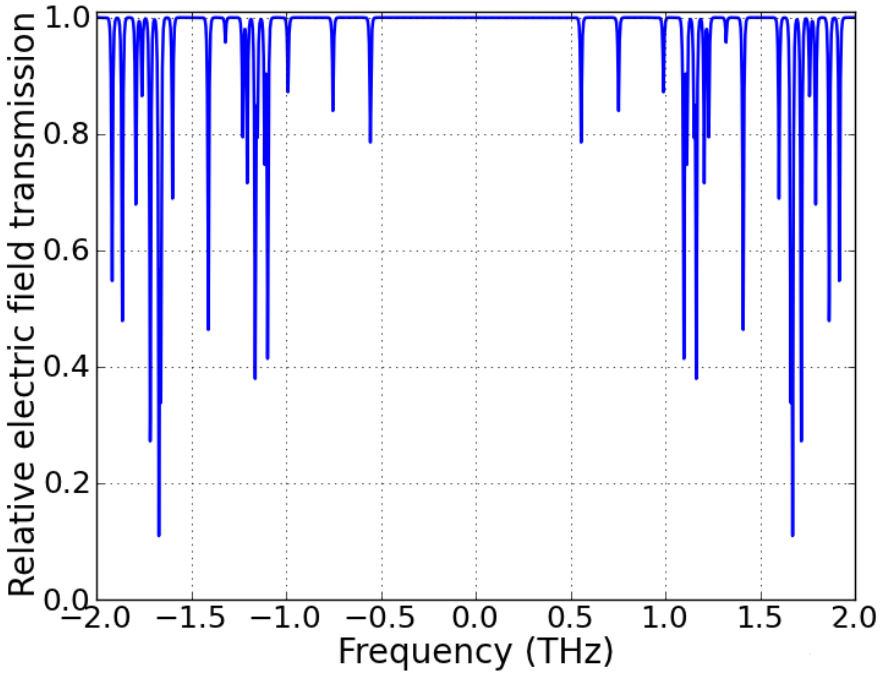

Figure 5.15. The transmission through water vapour, as a function of frequency.

Figure 5.16(b) shows the electric field as a function of time. It is obtained by finding the inverse Fourier transformation of the product of the numerical electric field $E(\omega)$ and the interpolated values of electric field transmitted through water vapour, both in frequency domain. Figure 5.16(a) shows the electric field as a function of time obtained using equation (3.60), which describes the electric field in the PC antenna as indicated in Figure 3.11. We

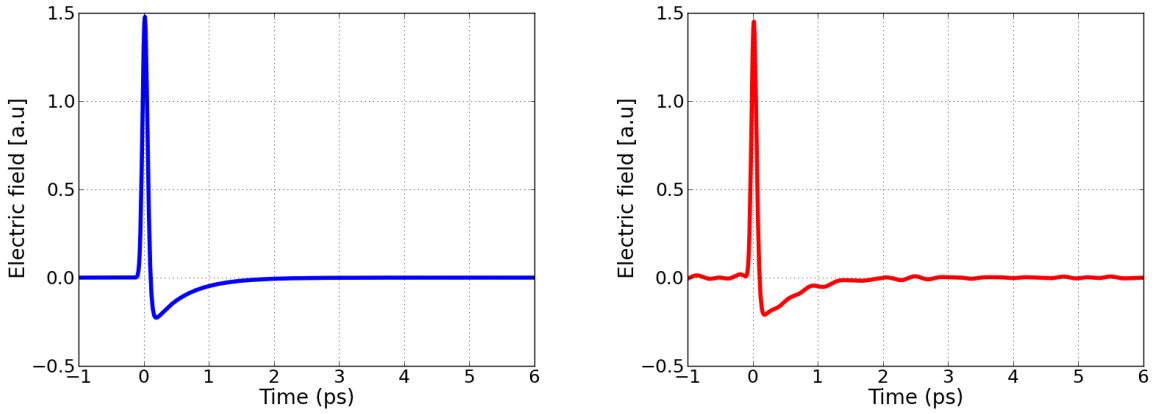

(a) (b)

Figure 5.16. (a) The electric field as a function of time from a PC antenna and (b) the electric field as a function of time through water vapour.

can see clearly the difference between the two figures. The small oscillations in Figure 5.16(b) are due to absorption by water vapour. These are the THz pulses obtained with and without water vapour respectively. The result of the simulation in Figure 5.16(b) is similar to the experimentally obtained electric field of a THz pulse in the time domain indicated in Figure 5.18(a).

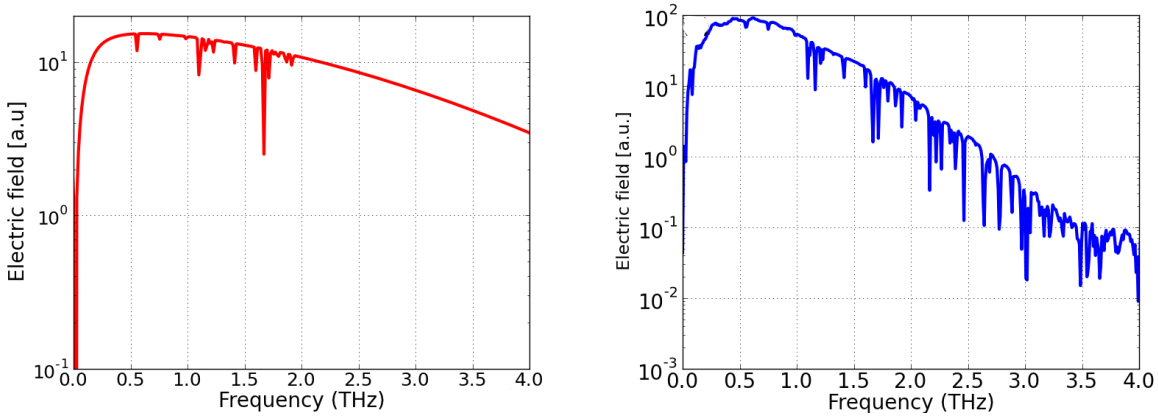

(a) (b)

Figure 5.17. (a) Simulated electric field through water vapour as a function of frequency, and (b) Experimentally measured electric field through water vapour as a function of frequency.

Figure 5.17 shows the comparison between the simulated electric field through water vapour and the experimentally measured electric field through water vapour (see Section 5.3). Note that absorption lines indicated on the Figure 5.17(a) are limited to the frequency range $0.4 - 2$ THz since our relative electric field transmission used is within that range. The position of the absorption lines in Figures 5.17(a) and 5.17(b) agree, even though the amplitudes do not. This is due to different experimental conditions.

5.3 Measurement of THz pulse through water vapour

All our measurements were performed using the Menlosystem Tera K8 system described in Section 4.2. Figure 5.18(a) shows a typical THz-pulse measurement from our setup described in Section 4.2. The pulse has only one single dominant oscillation followed by small oscillations. The small oscillations are due to absorption by the laboratory air humidity. In the experiment, we measured the electric field as a function of time. The corresponding spectrum as a function of frequency is given in Figure 5.18(b). The maximum of the spectrum is located at 0.45 THz. Similar work was done by Pradarutti, et al. [6]. The

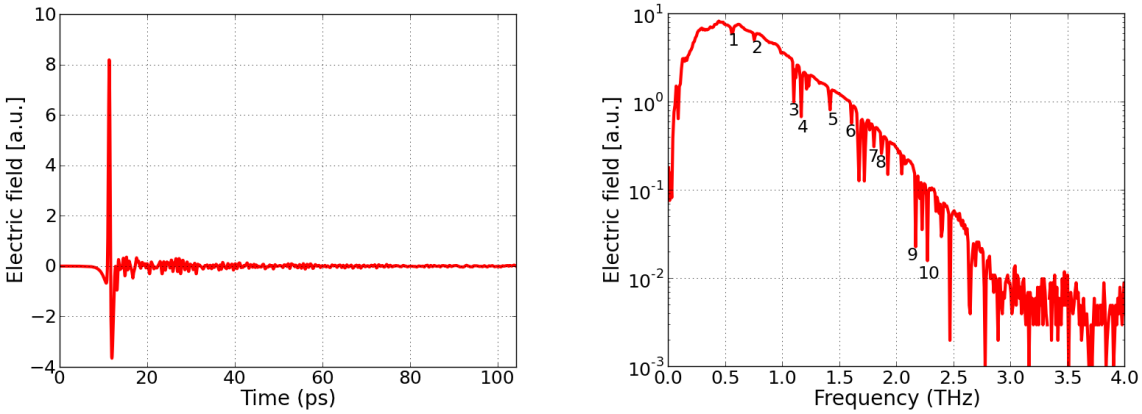

(a) (b)

Figure 5.18. (a) Waveform of the THz-pulse, (b) the corresponding FFT of the electric field.

sharp absorption lines of THz radiation by the water vapour can be clearly seen. These absorption lines are due to rotational transitions of water vapour molecules [45, 46, 47]. To check the calibration of our THz spectroscopy system, we use some selected absorption

lines, numerically marked in Figure 5.18(b). We use the frequencies of these absorption lines to obtain the corresponding wavenumbers and compare the results with data from Hall *et al.* [45]. Our experimentally measured values and literature values are presented in Table 5.1. The rotational transition of the absorption lines in Table 5.1, corresponds to the intermolecular rotational energy levels from the low state to the high state.

Line	f[THz] measured	$f \pm 0.09$ [cm^{-1}] measured	f[cm^{-1}] [45]	Rotational transition [45]
1	0.55	18.39	18.58	$1_{01} \longrightarrow 1_{10}$
2	0.75	25.08	25.09	$2_{02} \longrightarrow 2_{11}$
3	1.10	36.79	36.59	$3_{03} \longrightarrow 3_{12}$
4	1.16	38.80	38.79	$3_{12} \longrightarrow 3_{21}$
5	1.42	47.49	47.04	$5_{14} \longrightarrow 5_{23}$
6	1.60	53.51	53.46	$4_{04} \longrightarrow 4_{13}$
7	1.80	62.54	62.31	$5_{23} \longrightarrow 5_{32}$
8	1.87	62.58	62.87	$7_{52} \longrightarrow 8_{45}$
9	2.17	72.85	72.20	$2_{01} \longrightarrow 3_{13}$
10	2.22	74.25	74.11	$5_{05} \longrightarrow 5_{14}$

Table 5.1. Water vapour absorption lines in the THz range.

We graphically present the data to check the calibration of the spectrometer in Figure 5.19. Below is a plot of the literature values against the measured values with a linear fit, we obtained the standard deviation of ± 0.09 cm^{-1} between the measured and the literature data.

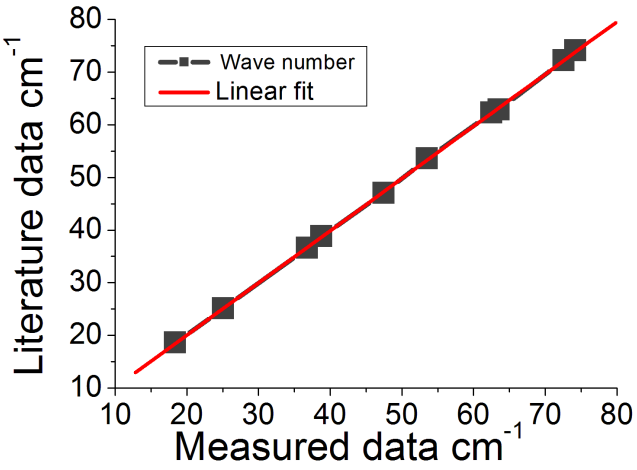

Figure 5.19. Comparison of measured wavenumber with literature (calculated) values.

5.4 Measurement of spectral resolution

To investigate the spectral resolution as function of time window[1], we repeat the measurement for different total time windows (TTW). We measure the electric field in time and calculate the frequency spectrum for the different time window measurements. We obtained the following measurements for the electric field and spectrum for different TTW's as shown in Figures, 5.20(a)–5.22(b).

[1]The time period considered best for starting and finishing the sampling of the THz electric field

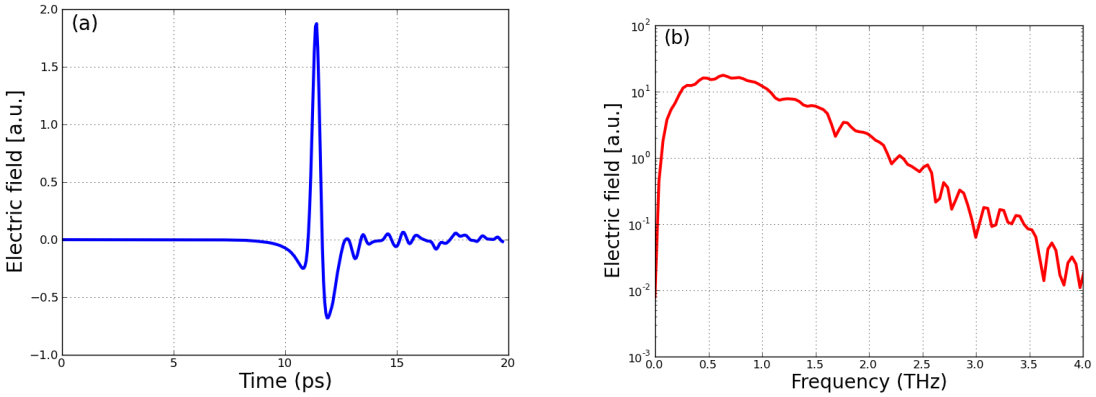

(a) The electric field as a function of time. (b) The electric field as a function of frequency.

Figure 5.20. (a) Waveform of the THz-pulse for TTW =20 ps, (b) the corresponding FFT of the electric field.

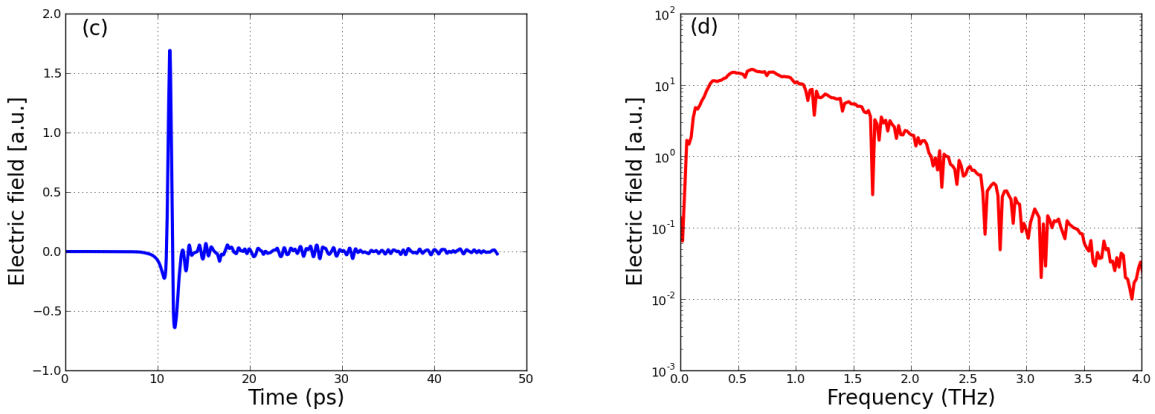

(a) The electric field as a function of time. (b) The electric field as a function of frequency.

Figure 5.21. (a) Waveform of the THz-pulse for TTW =47 ps, (b) the corresponding FFT of the electric field.

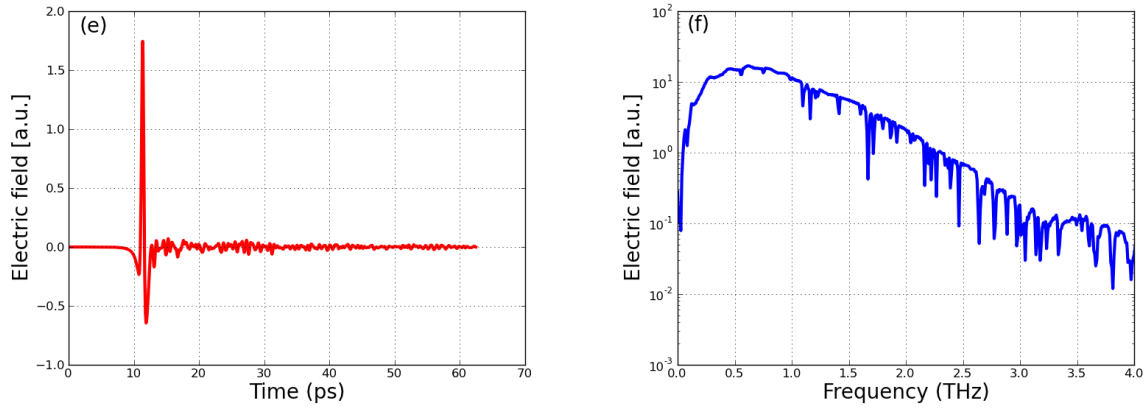

(a) The electric field as a function of time. (b) The electric field as a function of frequency.

Figure 5.22. (a) Waveform of the THz-pulse for TTW =62 ps, (b) the corresponding FFT of the electric field.

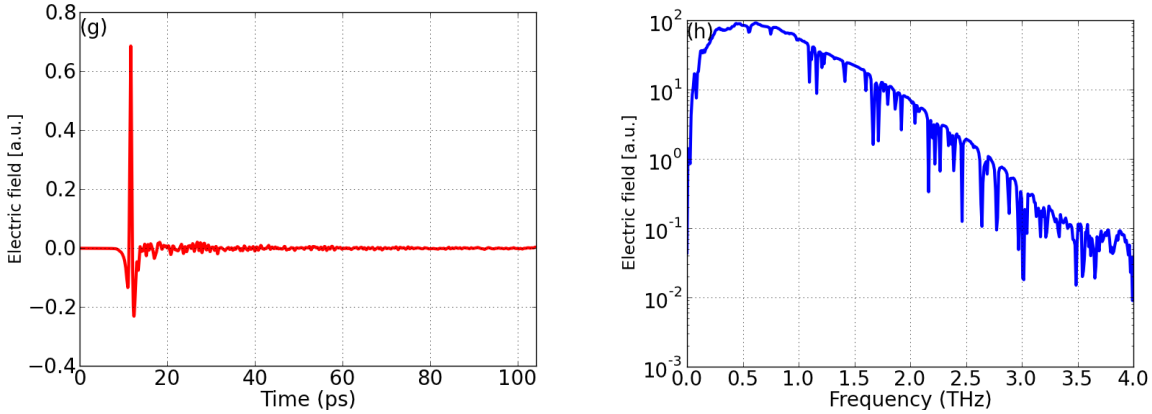

(a) The electric field as a function of time. (b) The electric field as a function of frequency.

Figure 5.23. (a) Waveform of the THz-pulse for TTW =100 ps, (b) the corresponding FFT of the electric field.

We investigate the resolution of the spectrometer using the technique of Full Width at Half Maximum (FWHM) of specific absorption lines. To determine the FWHM of an absorption line, we consider two base points (x_l, y_l) and (x_r, y_r) as illustrated in Figure 5.24. It is important to note that, the (successive) base points are not always on the same horizontal line. Using the base points (x_l, y_l) and (x_r, y_r) respectively together with (x_m, y_m), the bottom of the absorption line, we calculate the FWHM_1, FWHM_2 and take

their average. We do this because, considering only one case would result in biased values of the FWHM i.e. would be inclined to either a very low or very high value. We now demonstrate how the FWHM is calculated assuming $y_r < y_l$.

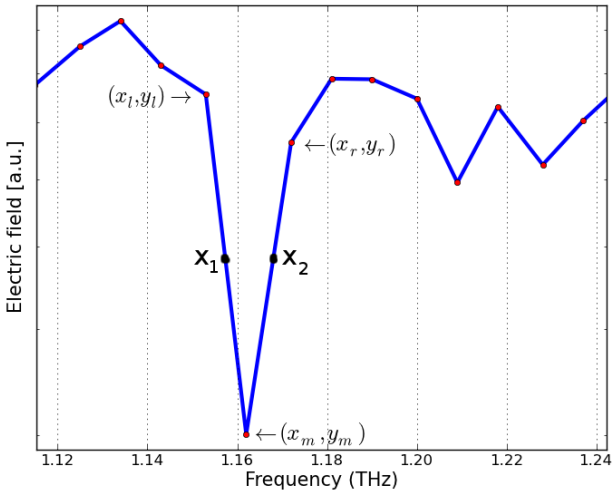

Figure 5.24. Sample of an absorption line at 1.162 THz

In this case, we calculate X_2, the FWHM with the base of the absorption line at (x_r, y_r). The height of the absorption line is $y_h = y_r - y_m$ and the y-coordinate at half maximum is given by

$$y = \frac{y_r + y_m}{2}. \tag{5.5}$$

If the horizontal line at half maximum has x coordinates x_1 and x_2 such that $x_1 < x_m < x_2$. Then x_1 and x_2 are respectively given by

$$x_1 = \frac{(y_r - y_m)(x_l - x_m)}{2(y_l - y_m)} + x_m, \tag{5.6}$$

$$x_2 = \frac{x_r + x_m}{2}. \tag{5.7}$$

Consequently FWHM, is given by the difference between the x_2 and x_1, as indicated below

$$\text{FWHM}_1 = \frac{(x_r - x_m)(y_l - y_m) + (y_r - y_m)(x_m - x_l)}{2(y_l - y_m)} > 0. \tag{5.8}$$

We now consider the second case with the base of the absorption line at (x_l, y_l).

$$x_1 = \frac{x_l + x_m}{2}, \tag{5.9}$$

$$x_2 = \frac{(y_l - y_m)(x_r - x_m)}{2(y_r - y_m)} + x_m, \tag{5.10}$$

$$\text{FWHM}_2 = \frac{(y_l - y_m)(x_r - x_m) + (x_m - x_r)(y_r - y_m)}{2(y_r - y_m)} > 0. \tag{5.11}$$

We calculate the full width at half maximum (FWHM) at frequencies 1.16 and 3.65 THz for all the varying total time windows (TTW), $20, 47, 62$ and 100 ps and the results are shown in Figures 5.25(a) and 5.25(b) below.

In Figures 5.25(a)–5.25(b), the FWHM decreases with total time window. For TTW ≥ 60 ps the FWHM dose not see to improve significantly.

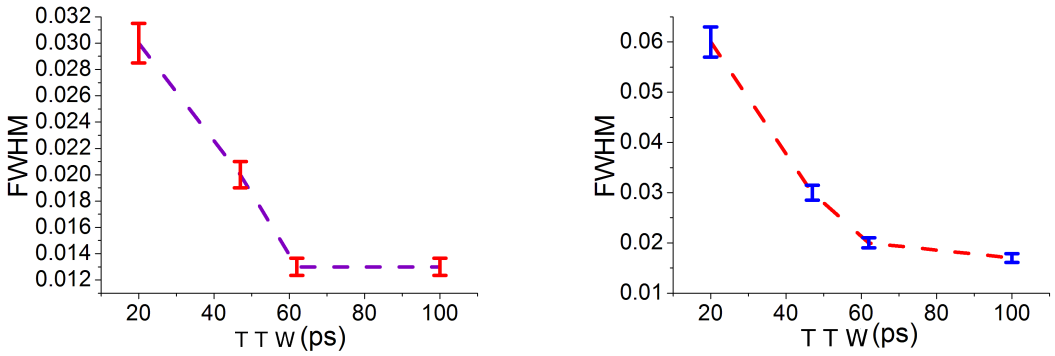

(a) (b)

Figure 5.25. FWHM as a function of TTW for same selected absorption lines at; (a) $\simeq 1.16$ THz and (b) $\simeq 3.65$ THz.

5.5 Measurement of the absorption coefficient and the refractive index of transparent materials.

The monochromatic electric field after propagating a distance z, in time t is given by [2]

$$E(z,t) = E_0 e^{i(Kz - \omega t)}, \tag{5.12}$$

where ω and K are angular frequency and the wave vector of the light, respectively, and E_0 is the amplitude. K is related to the wavelength λ through the relation

$$K = \frac{2\pi\tilde{N}}{\lambda} = \frac{\tilde{N}\omega}{c}, \tag{5.13}$$

where $\tilde{N}$ is the the complex index of refraction given by $\tilde{N} = n + ik$; n is the real index of refraction and k is the extinction coefficient (proportional to the absorption coefficient α of the media). We now substitute equation (5.13) into (5.12) to obtain

$$E(z) = E_0 e^{-\frac{k\omega z}{c}} e^{i(\frac{\omega n z}{c} - \omega t)}, \tag{5.14}$$

So the absorption coefficient of the medium through which the wave travels is $\alpha_E(\lambda) = \frac{2\pi k}{\lambda}$. The intensity of a light wave is proportional to the square of the electric field ($I \propto |E|^2$). The electromagnetic waves propagate through a homogeneous medium at a speed [2]

$$\nu = \frac{c}{n} = \frac{2d}{t}, \tag{5.15}$$

where d is the physical length of the medium such that $2dn$ is the "round trip" optical path length, c is the speed of light in free space and n is the refractive index of the medium. From equation (5.15), the time (t) is given by

$$t = \frac{2dn}{c}, \tag{5.16}$$

As an example of a transparent material we consider the propagation of a THz pulse through a 0.33 mm Si sample. To determine the refractive index of silicon, we measure the THz pulse (electric field) in the time domain with and without the sample (n-type doped silicon). We show the plots of the measurement in Figure 5.26. In Figure 5.26(b), there are three distinguishable peaks of the THz pulse. The first peak in time is the part of the pulse that passed through the Si sample once on the way to the detector, the second peak is the part of the pulse that underwent one back and forth reflection inside the sample (thus passing 3 times through the sample) before reaching the detector and the 3^{rd} peak is the part of the pulse that underwent 2 back and forth reflections in the samples. Therefore the time difference between any two of the peaks corresponds to one round trip time t in the sample.

Due to losses resulting from reflection at the interface, and the absorption and dispersion

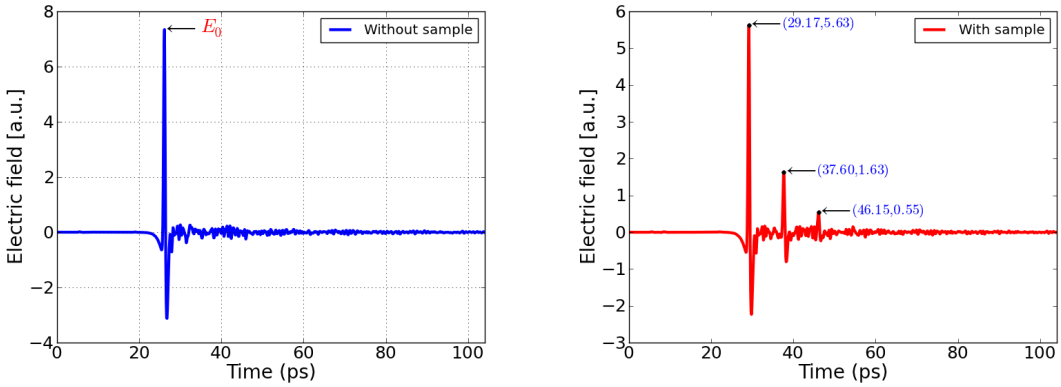

(a) (b)

Figure 5.26. (a) Waveform of the THz-pulse without sample and (b) the electric field with sample (silicon) of thickness = 0.33 mm .

in the sample which depend on frequency, the shape and magnitude of the pulse, outputs are changed [48]. We calculate the refractive index of silicon using equation (5.16) and the reflectance, R, using equation (3.44) to obtain $n = 3.835$ and $R = 0.34$ respectively. The refractive index of the silicon in THz range is 3.41 [2].

5.5.1 Determining the complex refractive index using the Fresnel equations

In this method, we consider a radiation incident on a material with thickness d. The reflectance R describes the reflection at the surfaces of the material. It is the ratio of the reflected energy to the energy incident on the material. The transmittance T is the transmitted energy to energy incident on the material. If there is no absorption or scattering at the surface, these two optical constants are such that $R + T = 1$ [49]. The absorption coefficient, α, quantifies the absorption of the incident energy by the material. Using Lambert-Beer's law describing optical intensity for an absorbing medium with reflectance R for the front and back surfaces, the transmittance is given by [49]

$$I = (1 - R)^2 e^{-\alpha d}.$$

In our spectroscopic measurement of the refractive index of silicon, we consider an electric field E_0 incident on the sample of thickness d. We represent the surfaces at which the

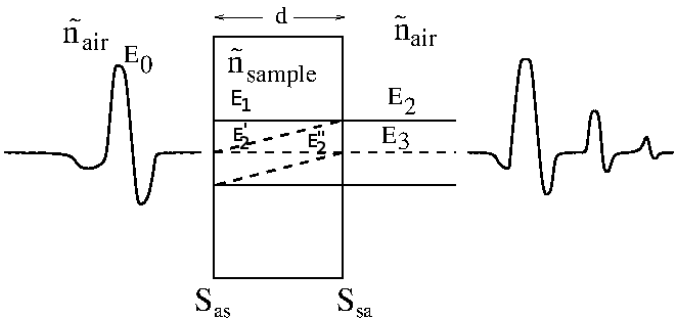

Figure 5.27. The multiple reflection at the sample interface.

electric field is incident and exits the sample by S_{as} and S_{sa}, respectively. We assume that on the surfaces of the sample, there is neither absorption nor scattering, but only reflection and transmission. The amplitude reflection coefficient is given by $r = \sqrt{R}$ at any surface. The amplitude transmission coefficient is given by $t_{as} = \sqrt{\frac{n_a}{n_s}T} = \sqrt{\frac{n_a}{n_s}(1-R)}$ for air to silicon, and $t_{sa} = \sqrt{\frac{n_s}{n_a}T} = \sqrt{\frac{n_s}{n_a}(1-R)}$ for silicon to air. However, $t_{sa}t_{as} = T = 1 - R$. The absorption of the electric field through the sample of thickness d is given by the factor $e^{\frac{-\alpha d}{2}}$. When the beam is incident on surface S_{as} with electric field E_0, it travels through the sample of thickness d with an electric field which decays with thickness and when arriving at surface s_{sa} is given by

$$E_1 = E_0 t_{as} e^{-\frac{\alpha d}{2}} = E_0 \sqrt{\frac{n_a}{n_s}(1-R)} e^{-\frac{\alpha d}{2}}, \tag{5.17}$$

with R, the reflectance of the sample and α, the absorption coefficient. At surface S_{sa}, part of the beam is transmitted and the rest is reflected. The corresponding electric field for the transmitted beam is given by

$$E_2 = E_0 t_{as} t_{sa} e^{-\frac{\alpha d}{2}} = E_0 (1-R) e^{-\frac{\alpha d}{2}}. \tag{5.18}$$

The electric field for the back reflected beam when arriving at surface S_{as} is

$$E_2' = E_0 t_{as} r e^{-\alpha d} = E_0 \sqrt{\frac{n_a}{n_s}(1-R)}\,(R)^{\frac{1}{2}}\, e^{-\alpha d}. \tag{5.19}$$

At surface S_{as}, part of the beam is transmitted and the rest is reflected. The corresponding electric field for the reflected beam is

$$E_2'' = E_0 t_{as} r^2 e^{-\frac{3\alpha d}{2}} = E_0 \sqrt{\frac{n_a}{n_s}(1-R)} R e^{-\frac{3\alpha d}{2}}. \tag{5.20}$$

After another transmission at surface S_{sa} the electric field is given by

$$E_3 = E_0 t_{as} r_2 t_{sa} e^{-\frac{3\alpha d}{2}} = E_0 (1-R) R e^{-\frac{3\alpha d}{2}}. \tag{5.21}$$

Combining equations (5.18) and (5.20) we obtain an expression for the reflectance R in terms of the absorption coefficient α, and the thickness d

$$R = \left(\frac{E_3}{E_2}\right) e^{\alpha d}. \tag{5.22}$$

Substituting (5.22) into (5.18), we obtain the following quadratic equation in terms of the absorption coefficient given as

$$\left(\frac{E_0 E_3}{E_2}\right) y^2 + E_2 y - E_0 = 0, \text{ with } \quad y = e^{\alpha d/2}. \tag{5.23}$$

Solving equation (5.23), with $E_0 = 7.3426$, $E_2 = 5.6306$, $E_3 = 1.6324$ indicated in Figures 5.26(a) and 5.26(b), we obtain the reflectance, R of the material as $R = 0.277$. Since the THz waves are incident on the silicon-air interface at near-normal incidence, the reflection coefficient is given by Fresnel's equation (3.44)

$$R = \left(\frac{n_{Si} - 1}{n_{Si} + 1}\right)^2. \tag{5.24}$$

The refractive index of silicon obtained from this calculation is $n_{Si} = 3.22$, reflectance $R = 0.277$ and the absorption coefficient is $\alpha_{\mathrm{Si}} = -0.046\mathrm{mm}^{-1}$(which is zero within the accuracy of the measurement).

To determine the refractive index of sapphire using our spectroscopy setup, we use the same model based on thickness of the sample and the time taken by the pulse to travel through the sample as described in Section 5.5. As indicated in Figure 5.28(b), the transient pulse $E_2 = 2.51$ a.u. which goes through sapphire is about 48% of the original pulse $E_0 = 5.22$ a.u. The sample of sapphire used was of thickness 1.87 mm and this could have contributed to the high absorption of the pulse by the sample, hence the low transmitted electric field.

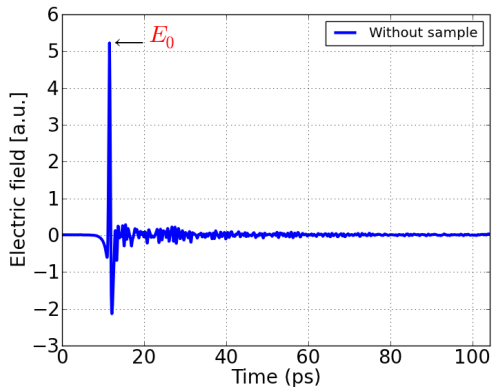

(a) The electric field as a function of time.

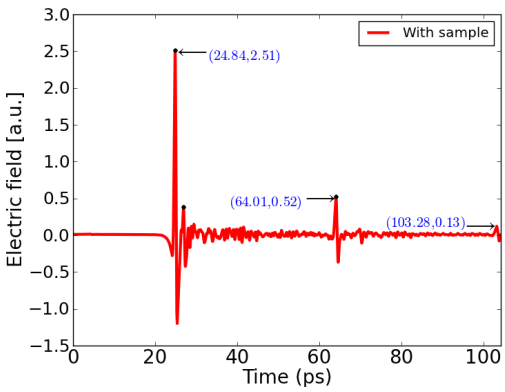

(b) The electric field as a function of time.

Figure 5.28. (a) Waveform of the THz-pulse without sample and (b) the electric field with a sample (Sapphire) of thickness = 1.87 mm .

We obtained a refractive index of sapphire as $n_{sap} = 3.18$. Using the alternative model in subsection 5.5.1 based on reflectance, transmittance and absorption of the radiation by the material and applied it on sapphire using $E_0 = 5.22$, $E_2 = 2.51$, $E_3 = 0.52$. we obtained the reflectance $R = 0.36$ and the refractive index of sapphire $n_{sap} = 4.03$, and the absorption coefficient is $\alpha_{\text{sap}} = 0.300$ mm^{-1}.

Our averaged experimentally obtained values of refractive index of silicon and sapphire by this method in THz range are 3.23 and 4.03, respectively. However, our results slightly deviate from the literature values (3.41 for silicon and 3.47 for sapphire), by 5% and 16% for silicon and sapphire, respectively. We give the summary of the comparison of two methods used for calculating the refractive indices for silicon and sapphire in Table 5.2.

	Literature	Method 1	Method 2
Silicon	3.41 [2, 7]	3.84 (13% higher than literature)	3.23 (5% lower than literature)
Sapphire	3.47 [2]	3.18 (8% lower than literature)	4.03 (16% higher than literature)

Table 5.2. Comparison between two methods used in finding the refractive indices

5.6 THz radiation spectrum in absence of water vapour

THz radiation is absorbed by water vapour molecules, therefore, the spectroscopy of materials results in a combination of spectra of the material and absorption lines in the frequency domain due to water vapour molecules [50]. However, the water vapour molecules can be removed from the path of the THz radiation by putting the optical setup in a vacuum chamber (this is the ideal case). Since a vacuum chamber is complicated to create, it can be approximated by enclosing the optical setup of the spectrometer in a box purged with dry air or a non-polar gas such as nitrogen [50]. , which does not have transitional energy levels in the THz range [50].

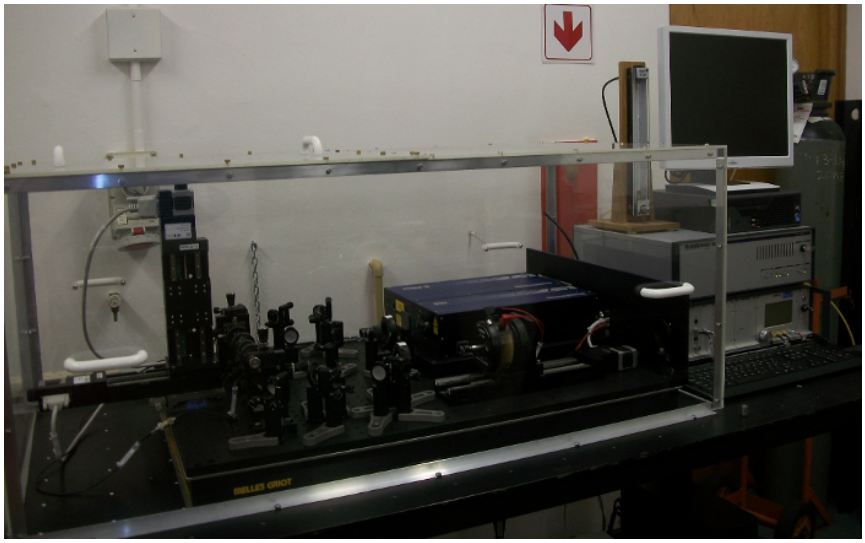

Figure 5.29. Experimental enclosed setup for generating and detecting THz radiation.

In our experiment to verify that water vapour absorbs THz radiation, we flushed nitrogen into the setup enclosed in a box. In our more elaborate procedure, we initially flushed nitrogen into the enclosed setup for 15 minutes at a pressure of 200kPa, before starting the THz measurement. We then started the measurement while still flushing the nitrogen and this continued throughout the process. Our results of electric field measurement as a function of time and frequency are shown in figures 5.30(a) and 5.30(b) respectively.

In Figure 5.30(b), we observed almost no absorption lines, since nitrogen does not have rotational absorption lines [50]. This is because acquiring rotational energy by absorbing

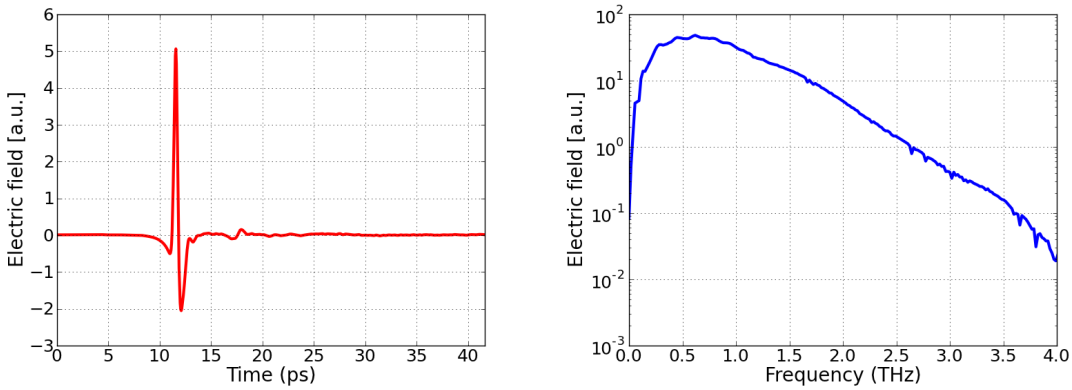

(a) The electric field as a function of time. (b) The electric field as a function of frequency.

Figure 5.30. (a) The electric field as a function of time, (b) the electric field as a function of frequency, for transmission through a N_2 atmosphere.

radiation in this range is forbidden by the quantum selection rule. The basis for this spectroscopic selection rule is the value of the integral of the transition moment function given by [51]

$$\mathcal{D} = \int_{-\infty}^{\infty} \Psi_i^{\dagger} \mu \Psi_j d\tau,$$

where Ψ_i and Ψ_j are the wavefunctions of the initial (i) and final (j) states of the spectral transitions and μ is the transition moment operator. If the value of the integral is zero, $(\mathcal{D} = 0)$ then transitions are forbidden. Otherwise, the transition is allowed / permitted [51]. The existence or non existence of rotational transition spectra of nitrogen in the THz range can be determined by using the selection rules for dipole radiation. For a molecule with three dimensional coordinate position (x, y, z), the components of the transition moment operator μ_x, μ_y, μ_z of the dipole moment change signs upon reflection at the origin. The components of the transition moment function are then given by

$$\mathcal{D}_x^{ij} = \int \psi_i^{\dagger} \mu_x \psi_j d\tau,$$
$$\mathcal{D}_y^{ij} = \int \psi_i^{\dagger} \mu_y \psi_j d\tau,$$
$$\mathcal{D}_z^{ij} = \int \psi_i^{\dagger} \mu_z \psi_j d\tau.$$

If both combining levels with eigenfunctions ψ_i and ψ_j respectively are of the same sign, the integrand will change sign for a reflection at the origin and so will the integrals. For the case

of homonuclear non-polar diatomic molecules with coordinates (x_1, y_1, z_1) and (x_2, y_2, z_2), upon exchange of the atoms, the dipole moment remains unchanged. A Nitrogen molecule is a non-polar homonuclear diatomic molecule. Therefore, its dipole moment is zero and no transition between the different rotational levels occurs and no infrared emission or absorption [51] occurs.

5.6.1 Background corrected spectrum of water vapour

In this technique we use two measurements. First, we measure the electric field through water vapour (E). Secondly, the electric field without water vapour (E'), both in the frequency domain. Theses measurements are such that the electric field (E) through water vapour is given by

$$E(d) = E_0 e^{-\alpha d}, \tag{5.25}$$

and electric field without water vapour E' is given by

$$E' = E_0. \tag{5.26}$$

The absorbance is calculated by taking the logarithm of the ratio of the spectrum without water vapour to the spectrum with water vapour in the path of the THz radiation such that

$$-\log(E/E^{'}) = \alpha d. \tag{5.27}$$

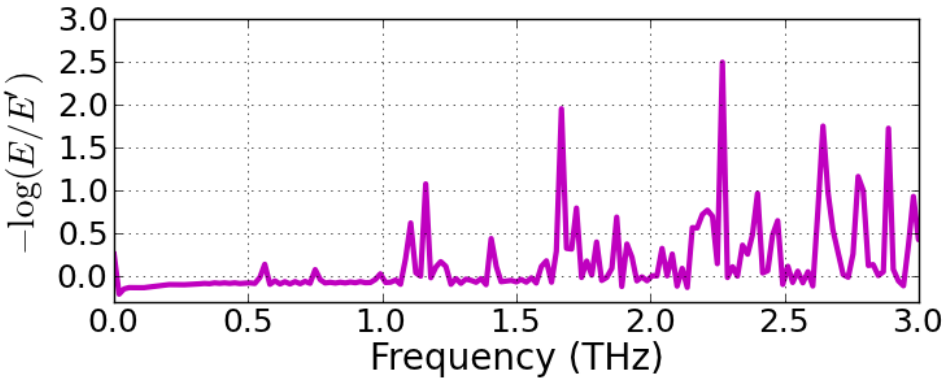

Figure 5.31. Background corrected spectrum of water vapour from 0.0 to 3.0 THz.

5.7 THz imaging

Among the applications of THz spectroscopy is the generation of two-dimensional images of an object using THz radiation [52]. THz radiation can be transmitted through most non-metallic and non-polarizing materials, for example semiconductors, plastics, e.t.c [30]. Therefore, obtaining images of the inside of these materials with THz radiation is possible,

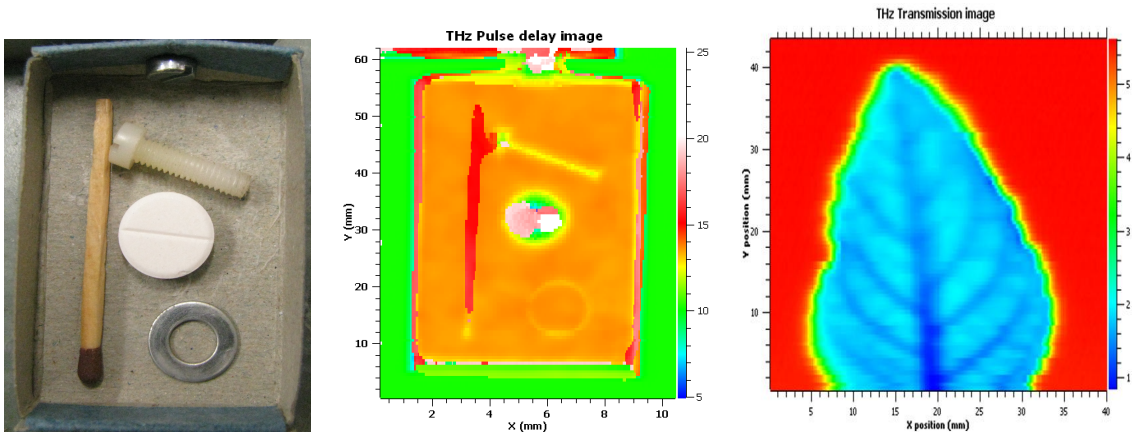

(a) (b) (c)

Figure 5.32. Photo of an open matchbox and its contents (a), a THz wave image when the matchbox was imaged while closed (b) and THz wave image of leaf (c). [For clear interpretation of these images with regard to colour, we refer the reader to the electronic version of this document.]

while it is usually difficult or impossible with optical light [30]. The THz-TDS image

contains spectroscopic information. Therefore, it carriers more information compared to a typical 2-D image with the same number of pixels [2]. This is because in the THz image, each pixel contains a whole waveform in time domain. In this Subsection, we show the principle of THz imaging using our spectroscopy system using a matchbox with contents and a leaf.

Figure 5.32(a) shows a photographic image of a matchbox (containing a matchstick, a plastic screw, a metal ring and a commercial paracetamol tablet). Figure 5.32(b) shows the THz pulse delay image of a closed matchbox with its contents as false colour representation. In this figure the contents, i.e the wood of the matchstick and its sulphur head, the plastic screw, the tablet and the metallic ring that is reflective, can be clearly distinguished. All the contents of the matchbox are transparent for THz radiation except the metallic ring is reflective for THz radiation. The colour bar in Figure 5.32(b) indicates decreasing refractive index of the materials. The dense blue colour corresponds to low refractive index (closer to that of air) whereas the top white colour corresponds to high refractive index. Since the refractive index is proportional to time delay [53], the materials with high refractive index in the THz range have high delay for the THz radiation.

Figure 5.32(c) shows the transmission image of the leaf. In transmission imaging, the nature of the image is determined by the transmission power of the radiation. The transmitted THz power amplitude also determines the colour scale of the image and this is strongly related to the moisture content at each point of the sample [54] . In the image of the leaf Figure 5.32(c), the dark blue color on the scale indicates the regions with high moisture content, typically the midrib and the veins. In these region, the THz radiation is strongly absorbed.

Chapter 6

Summary

In this thesis, we studied the general theory of the electrical circuit of a THz-TDS system. We showed that the current across the capacitor in the RLC circuit is oscillatory for under damped oscillation and non oscillatory for both critical and over damped cases, Figure 2.2. The electric field, being directly proportional to the time derivative of current, takes an opposite y-direction to that of the current but with the same "sinusoidal" behaviour as a function of time. The general principle of pump-probe method was discussed in Section 3.6 and the principle of THz-TDS in Section 3.7. We described THz as an electromagnetic wave using Maxwell's equations in Section 3.1 and obtained the fundamental equation (3.22) for generation and propagation of electromagnetic waves of which THz is inclusive. We described various techniques for generating THz radiation namely,

1. "frequency down conversion" from nonlinear media THz sources resulting in both broadband and CW THz radiation, and

2. "frequency up conversion" from accelerating electrons THz sources such as photocurrent in semiconductors and free electrons in vacuum, also resulting in both broadband and CW THz radiation.

In Section 3.3, we described the photoconductive antenna as a THz emitter and detector. We showed that the electric field through the antenna is directly proportional to the time derivative of the photocurrent in the photoconductive gap of the PC antenna, equation (3.51). The explicit expression of the proportionality relation was indicated in equation

(3.60) and the graphical representation in Figure 3.11. We outlined some of the desirable properties of the photoconductive materials, which include short carrier lifetime, high carrier mobility and high breakdown voltage. The summary of the materials used in PC- antennas was given in Table 3.2, highlighting LT-GaAs as the most commonly used material.

We gave a brief description of the experimental setup of the THz-TDS system used in Section 4.1, and THz transparent materials in Subsection 4.3. We indicated that the desirable properties of a good window material are good transmission in both the THz and visible range of the electromagnetic spectrum. TPX being transparent in both THz and the visible range, is cited as one of the most favourable window materials.

In Chapter 5, we presented the numerical simulations of voltage across a capacitor and electric field emitted by a RLC circuit for different damping cases and for both constant and variable resistance, Figures 5.1–5.2. We simulated the absorption and transmission properties of a material by multiplying the voltage across the capacitor by a generated transfer function containing absorption and transmission bands. Our results in both frequency and time domains are indicated in Figures 5.3–5.5. The corresponding electric field measurements for the different absorption and transmission bands are indicated in Figures 5.8–5.10.

We experimentally measured the THz pulse in time domain that has passed through water vapour in Figure 5.16(b), and corresponding Fourier transformation of the electric field in frequency domain, Figure 5.16(a), was used to verify the calibration of the spectroscopic system. Our results for the experimental absorption lines and the theoretically calculated lines are presented in Table 5.1. The observed standard deviation of our measurements from the theoretical values is 0.09 cm^{-1}.

We also investigated the spectral resolution as a function of time window using the full width at half maximum (FWHM) of specific absorption lines and our results are presented in Section 5.4 indicating that, the resolution improves with increase in total time window. However, for time windows beyond 60 ps, the resolution does not improve significantly.

6.1 Future Work

We can use THz-TDS to measure the dielectric and optical properties of materials such as liquids, gases, semiconductors and biological materials. However, not much has been done for thin films (nanometer to micrometer) of materials. There is enough evidence to believe that the dielectric and optical properties of a variety of thin film materials such as SiO_2 can be characterised within the THz range if the thickness of the material is comparable to the wavelength of the THz wave. But this needs to be studied and experimentally verified [55].

Bibliography

[1] H J CHA, Y U Jeong, S H Park, and R C Lee. Transmission property measurements of crystal quartz and plastic material in the terahertz region. *Korean Physical Society*, 49:345–358, 2006.

[2] Y-S Lee. *Principles of terahertz, science and technology.* Springer, 2009.

[3] X-C Zhang and J Xu. *Introduction to THz Wave Photonics.* Springer Science + Business Media, LLC, 2010.

[4] Z Wang. Generation of terahertz radiation via nonlinear optical methods. *IEEE. Trans. Geosci. Remote Sens.*, 1:1–5, 2001.

[5] K Dobroiu, C Otani, and K Kawase. Terahertz wave sources and imaging applications. *Meas. Sci. Tenchnol.*, pages 161–174, 2006.

[6] B Pradarutti, G Mattäus, S Riehemann, G Notni, S Nolte, and A Tünnermann. Advanced analysis concepts for terahertz time domain imaging. *Optics Communication.*, 279:248–254, 2007.

[7] D L Woolard, W R Leorop, and M S Shur, editors. *Terahertz sensing technology*, volume 1. World Scientific Publishing Co. Pte. Ltd., 2003.

[8] F D Bruner, A Schneider, and P Günter. Terahertz time domain spectrometer for simultaneous transmission and reflection measurements at normal incidence. *Optical Society of America*, 17, 2009.

[9] M T Reiten. *Spatially resolved terahertz propagation.* PhD thesis, Oklahoma State University, 2006.

[10] S Wietzke, C Jansen, T Jung, M Reuter, B Baudrit, M Bastian, S Chantterjee, and M Koch. Terahertz time-domain spectroscopy and a tool to monitor the glass transition in polymers. *Optical Society of America.*, pages 19006–19014, 2009.

[11] Applied Research and Photonics. Terahertz spectroscopy brings new dawn of biological research. available from `http://arphotonics.net`, 2008.

[12] M Hoffmann. *Novel techniques in THz-time-domain-spectroscopy.* PhD thesis, Albert-Ludwigs-Universität, 2006.

[13] J Zhang, Y Hong, S L Braunstein, and K A Shore. Terahertz pulse generation and detection with LT-GaAs photoconductive antenna. *IEE proc. Optoelectron*, 151:98–101, 2004.

[14] M. Tonouchi. Cutting-edge terahertz technology. *Nat. Photonics.*, 1:97–105, 2007.

[15] K Humphreys, J P Loughran, M Gradziel, W Lanigan, T Ward, J A Murphy, and C OŚullivan. Medical applications of terahertz imaging: a review of current technology and potential applications in Biomedical Engineering. *IEEE EMBS.*, pages 1302–1305, 2004.

[16] V P Wallace, B C Cole, R M Woodward, R J Pyel, and D A Amone. Biomedical applications of terahertz technology. *IEEE*, pages 308–309, 2002.

[17] D Halliday, R Resnick, and J Walker, editors. *Fundamentals of physics extended with modern physics.* John Wiley & Sons, Inc, *fourth* edition, 1993.

[18] S Madhu. *Linear circuit analysis.* Prentice-Hall, Inc, 1988.

[19] W Knap, M Dyakonov, D Coquillat, F Teppe, N Dyakonova, J Łusakowski, K Karpierz, M Sakowicz, G Valusis, D Seliuta, I Kasalynas, A El Fatimy, Y Meziani, and T Otsuji. Field effect transistors for terahertz detection: Physics and first imaging applications. *J. Infrared Millim. TE*, 30:1319–1337, 2009.

[20] J F James, editor. *A student's guide to Fourier transforms.* Cambridge University press, 2002.

[21] J A Weil. A review of electron spin spectroscopy and its application to the study of paramagnetic defects in crystalline quartz. *Phys Chem Minerals*, 10:149–165, 1984.

[22] J Amster. Fourier transform mass spectrometry. 37:1325–1337, 1996.

[23] J L Koenig. Application of fourier transform infrared spectroscopy to chemical systems. *Appl. Spectrosc.*, 29:293–308, 1975.

[24] D J Griffiths and R College, editors. *Introduction to electrodynamics*. Prentice-Hall & , Inc, third edition, 1999.

[25] Stefan Gorenflo. *A Comprehensive Study of Macromolecules in Composites using Broadband Terahertz Spectroscopy*. Albert-Ludwigs-University ., 2010. Phd.

[26] F Graham Smith, Terry A King, and Dan Wilkins. *Optical and Photonics an Introduction*. John Wiley & Sons ,Inc., 2007.

[27] N Numan. *Optical fibres*. African Institute for mathematical Science (AIMS)., 2010. Diploma.

[28] M Tani, Y Hirota, C T Que, S Tanaka, R Hattori, M Yamaguchi, S Nishizawa, and M Hangyo. Novel terahertz photoconductive antennas. *Int. J. Infrared Millimeter Waves*, 27:531–546, 2006.

[29] A Rostami, H Rasooli, and H Bagban. *Terahertz technology fundamentals and applications*. Springer-Verlag Berlin Heidelberg, 2011.

[30] M Tani, M Herrmanna, and K Sakai. Generation and detection of terahertz radiation with photoconductive antennas and its application to imaging. *Meas. Sci. Technol*, 13:1739–1745, 2002.

[31] MenloSystems. THz-antennas for 800 nm: The solution for free-space THz systems. available from `http://www.menlosystems.com/home/products.html`.

[32] K Sakai. *Terahertz optoelectronics*. Springer-Verlag Berlin Heidelberg, 2005.

[33] W L Chan, J Deibel, and D M Mittleman. Imaging with terahertz radiation. *Rep. Prog. Phys.*, 70:1325–1379, 2007.

[34] W Demtróder. *An introduction to atomic-, molecular-and quantum-physics*. Springer-Verrlag Berlin Heidelberg, 2006.

[35] D L Andrews and A A Bemitov, editors. *An introduction to laser spectroscopy*. Plenum Press, New York, 1995.

[36] C Rulliere, editor. *Femtosecond laser pulse*. Springer Science, Business Media, Inc, second edition, 2005.

[37] K Wang, D M Mittleman, N C J van der Valk, and P C M Planken. Antenna effects in terahertz apertureless near-field optical microscopy. *Appl. Phys. Lett.*, 85:2715–2717, 2004.

[38] TYDEX. `http://www.tydexoptics.com/products/thz_optics/thz_materials/`.

[39] S D Ganichev and W Prettl. *Intense terahertz excitation of semiconductors*. Oxford university press, 2006.

[40] M Fox. *Optical properties of solids*. Oxford University Press, 2001.

[41] B J Thompson. *Terahertz spectroscopy principles and applications*. Taylor & Francis Group, LLC, 2008.

[42] D R Lide, editor. *The Handbook of chemistry and physics*. CRC Press, LLC, 84^{th} edition, 2004.

[43] T Chibuye, C G Ribbing, and E Wäckelgard. Reststrahlen band studies of polycrystralline beryllium oxide. *Optical Society of America*, 33:5975–5981, 1994.

[44] A Wagner-Gentner, U U Graf, D Rabanus, and K Jacobs. Low loss thz window. *Infrared Phys. Technol.*, 48:249–253, 2006.

[45] R T Hall, D Vrabec, and J M Dowling. A high-resolution, far infrared double-beam lamellar grating interferometer. *J. Opt. Soc. Am.*, 5:1147–1158, 1966.

[46] P U Jepsen, R H Jacobsen, and S R Keiding. Generation and detection of terahertz pulses from biased semiconductor antennas. *J. Opt. Soc. Am.*, 13:2424–2436, 1996.

[47] R A Cheville and D G Grischkowsky. Far-infrared foreign and self-broadened rotational line widths of light-temperature water vapor. *J. Opt. Soc. Am.*, 16:317–322, 1999.

[48] M van Exter and D Grischkowsky. Carrier dynamics of electrons and holes in moderately doped silicon. *Physical Review B*, 41:12140–12149, 1990.

[49] M Fox. *Optical properties of solids*. Oxford university press Inc, New York, 2001.

[50] W Withayachumnankul, B M Fischer, S P Mickan, and D Abbott. Removal of water-vapor-induced fluctuations in T-ray signals: A preliminary study. *Proc. of SPIE*, 6603: 1–12, 2007.

[51] G Herzberg. *Molecular spectra and molecular structure*. D. Van Nostrand company, Inc, second edition, 1950.

[52] B B Hu and M C Nuss. Imaging with terahertz waves. *Opt. Lett.*, 20:1716–1720, 1995.

[53] J W Handley, A J Fitzgerald, E Berry, and R D Boyle. Wavelet compression in medical terahertz pulsed imaging. *Phys. Med. Biol.*, 47:3885–3892, 2002.

[54] D M Mittleman, R H Jacobsen, and M C Nuss. Tray imaging. *Appl. Spectrosc.*, 2: 679–692, 1996.

[55] K S Lee, T Ming Lu, and X C Zhang. Tera tool. *IEEE Circuits & devices Magazine*, pages 23–28, 2002.